

1 **Arctic Sea-Ice Reemergence: The Role of Large-Scale Oceanic**
2 **and Atmospheric Variability**

3 MITCHELL BUSHUK, * DIMITRIOS GIANNAKIS, AND ANDREW J. MAJDA

Courant Institute of Mathematical Sciences, New York University, New York, New York

* *Corresponding author address:* Mitch Bushuk, Center for Atmosphere Ocean Science, Courant Institute of Mathematical Sciences, New York University, 251 Mercer Street, New York, NY, 10012.

E-mail: bushuk@cims.nyu.edu

ABSTRACT

4
5 Arctic sea-ice reemergence is a phenomenon in which spring sea-ice anomalies are positively
6 correlated with fall anomalies, despite a loss of correlation over the intervening summer
7 months. This work employs a novel data analysis algorithm for high-dimensional multivariate
8 datasets, coupled nonlinear Laplacian spectral analysis (NLSA), to investigate the regional
9 and temporal aspects of this reemergence phenomenon. Coupled NLSA modes of variability
10 of sea-ice concentration (SIC), sea-surface temperature (SST), and sea-level pressure (SLP)
11 are studied in the Arctic sector of a comprehensive climate model and in observations.
12 It is found that low-dimensional families of NLSA modes are able to efficiently reproduce
13 the prominent lagged correlation features of the raw sea-ice data. In both the model and
14 observations, these families provide an SST–sea-ice reemergence mechanism, in which melt
15 season (spring) sea-ice anomalies are imprinted as SST anomalies and stored over the summer
16 months, allowing for sea-ice anomalies of the same sign to reappear in the growth season
17 (fall). The ice anomalies of each family exhibit clear phase relationships between the Barents-
18 Kara Seas, the Labrador Sea, and the Bering Sea, three regions that comprise the majority
19 of Arctic sea-ice variability. These regional phase relationships in sea ice have a natural
20 explanation via the SLP patterns of each family, which closely resemble the Arctic Oscillation
21 and the Arctic Dipole Anomaly. These SLP patterns, along with their associated geostrophic
22 winds and surface air temperature advection, provide a large-scale teleconnection between
23 different regions of sea-ice variability. Moreover, the SLP patterns suggest another plausible
24 ice reemergence mechanism, via their winter-to-winter regime persistence.

1. Introduction

Arctic sea ice is a sensitive component of the climate system, with dynamics and variability that are strongly coupled to the atmosphere and ocean. This sensitivity is evident in the recent precipitous decline in September sea-ice extent, of roughly 9% per decade since 1979 (Stroeve et al. 2007; Serreze et al. 2007). Trends in sea-ice extent are negative for all months of the year and all Arctic regions except for the Bering Sea (Cavalieri and Parkinson 2012). In addition to these strong trends, Arctic sea ice also exhibits large internal variability. Studies using comprehensive climate models have estimated that 50-60% of recent Arctic sea-ice changes can be attributed to externally forced trends, with the remainder resulting from internal variability in the climate system (Kay et al. 2011; Stroeve et al. 2012). Therefore, the challenge of making accurate projections of future Arctic sea-ice conditions crucially hinges on: (1) quantifying the sea-ice response to changes in external forcing (i.e., greenhouse gas forcing) and (2) understanding the nature and magnitude of internal variability in the coupled ice-ocean-atmosphere system. This study will focus on the latter.

The Arctic regions of interest in this study are shown in Fig. 1. The leading empirical orthogonal function (EOF) of observational Arctic sea-ice concentration (SIC) exhibits strong out-of-phase anomalies between the Labrador and Greenland-Barents Seas and weaker out-of-phase anomalies between the Bering Sea and Sea of Okhotsk (Deser et al. 2000). Regression of sea level pressure (SLP) onto the corresponding principal component (PC) yields a spatial pattern which closely resembles the Arctic Oscillation (AO, Thompson and Wallace 1998), the leading pattern of SLP variability north of 20°N. Deser et al. (2000) observe a connection between the low-frequency (interannual to decadal) variability of the atmosphere and the low-frequency variability of sea-ice. In particular, they find that the AO and its associated geostrophic winds are physically consistent with the ice anomalies of the leading SIC mode, suggesting that atmospheric circulation anomalies force sea-ice anomalies. These winds have thermodynamic and dynamic effects on sea ice via advection of surface air temperature and ice advection. Many other studies have analyzed sea-ice variability in

52 the context of the AO, finding that the AO affects sea ice on a wide range of time scales
53 ranging from seasonal (Serreze et al. 2003) to decadal (Rigor et al. 2002; Rigor and Wallace
54 2004; Zhang et al. 2004). These studies suggest that a “high-index” AO produces an Ekman
55 divergence, leading to reductions in sea-ice thickness and concentration. This process has
56 been proposed as a mechanism for the recent decline in Arctic sea ice.

57 Others have questioned the efficacy of the AO as a predictor for sea-ice changes (Maslanik
58 et al. 2007), suggesting that other patterns of large-scale atmospheric variability may play
59 a more important role. In particular, an SLP pattern known as the Arctic Dipole Anomaly
60 (DA) has drawn considerable recent attention (Wu et al. 2006; Wang et al. 2009; Tsuk-
61 ernik et al. 2010; Overland and Wang 2005, 2010; Watanabe et al. 2006). The DA exhibits
62 opposite-signed SLP anomalies between the Eastern and Western Arctic, which drive strong
63 meridional winds. These winds act to enhance (reduce) sea-ice export from the Arctic basin
64 through Fram Strait when the DA is in positive (negative) phase. Recent record lows in
65 summer sea-ice extent generally correspond to years in which the DA index was positive
66 (Wang et al. 2009). DA-like SLP patterns have also been associated with the large inter-
67 nal variability observed in the sea-ice component of the Community Climate System Model
68 Version 3 (CCSM3, Collins et al. 2006; Wettstein and Deser 2014). Other studies have sug-
69 gested that the location and frequency of storms (Screen et al. 2011), and the phase of the
70 Pacific-North-America (PNA) pattern (L’Heureux et al. 2008) also play an important role
71 in setting the summer sea-ice minimum.

72 The PCs corresponding to large-scale atmospheric patterns, such as the AO and DA, are
73 quite noisy and contain significant spectral power at time scales ranging from monthly to
74 decadal. A typical approach has been to initially low-pass filter the atmospheric component
75 (by forming annual or winter means), as a way of smoothing out these PCs and emphasizing
76 interannual to decadal variability. Besides the studies already cited, a large number of works
77 have analyzed the impact of this low-frequency atmospheric variability on Arctic sea ice
78 (Walsh et al. 1996; Proshutinsky and Johnson 1997; Mysak and Venegas 1998; Yi et al.

79 1999; Johnson et al. 1999; Deser et al. 2000; Polyakov and Johnson 2000; Moritz et al. 2002).
80 These studies emphasize that sea-ice regimes are modulated by low-frequency atmospheric
81 circulation regimes.

82 The variability of Arctic sea ice is also strongly coupled to sea surface temperature
83 (SST) variability (e.g., Francis and Hunter 2007). Blanchard-Wrigglesworth et al. (2011)
84 proposed a mechanism for sea-ice–SST co-variability, in which sea-ice and SST anomalies
85 trade off, allowing for unexpected “memory” effects in sea ice. These memory effects were
86 termed “sea-ice reemergence”, inspired by the similar North Pacific and North Atlantic SST
87 phenomena (Alexander et al. 1999; Timlin et al. 2002; de Cotlogon and Frankignoul 2003).
88 Sea-ice reemergence is a lagged correlation phenomenon, in which spring sea-ice anomalies
89 are positively correlated with fall sea-ice anomalies, despite a loss of correlation over the
90 intervening summer months. There is also a similar, but weaker, reemergence between
91 fall sea-ice anomalies and anomalies the following spring. The spring-fall mechanism of
92 Blanchard-Wrigglesworth et al. (2011) suggests that spring sea-ice anomalies imprint SST
93 anomalies of opposite sign, which persist over the summer months. During the fall, ice grows
94 southward and interacts with these SST anomalies, reproducing ice anomalies of the same
95 sign as the spring. This reemergence mechanism has been observed in the North Pacific sector
96 in CCSM3 model output and observations (Bushuk et al. 2014). Deser et al. (2002) note a
97 similar winter-to-winter persistence of sea-ice anomalies in the Labrador Sea, and propose
98 an atmospheric mechanism in which sea-ice anomalies persist due to persistent large-scale
99 atmospheric circulation regimes.

100 Sea-ice reemergence may also have implications for sea-ice predictability. Day et al. (2014)
101 found that sea-ice forecast skill was strongly dependent on initialization month, with certain
102 months exhibiting a slower decay of forecast skill than others. The authors suggested that
103 this initialization month dependence was attributable to sea-ice reemergence mechanisms.
104 Day et al. (2014) also examined sea-ice reemergence in five global climate models (GCMs)
105 and observations, finding robust reemergence signals, of varying strength, across all models

106 and a weaker reemergence signal in the observational record.

107 In this study, we examine the coupled variability of Arctic SIC, SST, and SLP using
108 nonlinear Laplacian spectral analysis (NLSA), a recently developed data analysis technique
109 for high-dimensional nonlinear time series (Giannakis and Majda 2012a,b, 2013, 2014). The
110 NLSA algorithm is a nonlinear manifold generalization of singular spectrum analysis (SSA,
111 Broomhead and King 1986; Vautard and Ghil 1989; Ghil et al. 2002). SSA is also commonly
112 referred to as extended empirical orthogonal function (EEOF) analysis. Here, we apply
113 the multivariate version of the NLSA algorithm, coupled NLSA (Bushuk et al. 2014), which
114 provides a scale-invariant analysis of multiple variables with different physical units. Coupled
115 NLSA yields spatiotemporal modes, analogous to EEOFs, and temporal modes, analogous to
116 PCs. These modes are constructed using a set of empirically derived Laplacian eigenfunctions
117 on the nonlinear data manifold and, unlike linear approaches, do not maximize explained
118 variance. Compared to linear techniques, NLSA (and other related nonlinear methods; Berry
119 et al. 2013) provide superior time-scale separation and are able to effectively capture low-
120 variance modes that may have important dynamical significance. These low-variance modes
121 are known to be crucial in producing accurate representations of nonlinear dynamical systems
122 (Aubry et al. 1993; Giannakis and Majda 2012b), and in the present context, are efficient in
123 explaining reemergence phenomena (Bushuk et al. 2014).

124 We use coupled NLSA modes to study the basin-wide and regional characteristics of
125 Arctic sea-ice reemergence in a comprehensive climate model and observations. We com-
126 pute modes using CCSM3 model output from a 900-year equilibrated control integration.
127 Modes are also obtained for the 34-year observational record, using SIC and SST data from
128 the Met Office Hadley Center Sea Ice and Sea Surface Temperature (HadISST) dataset and
129 Era-Interim SLP reanalysis data. No preprocessing of the data is required, enabling simulta-
130 neous extraction of interannual, annual, and semiannual patterns of variability. Using these
131 modes, we identify low-dimensional families which efficiently describe sea-ice reemergence.
132 These families capture a significant portion of the reemergence signal, and have the sur-

133 prising property of being relatively low-variance. The families also reveal time-dependent
134 aspects of reemergence, which were not accessible in previous studies. The SST and SIC
135 modes of each family exhibit an SST–sea-ice reemergence mechanism consistent with that
136 of Blanchard-Wrigglesworth et al. (2011). Interannual components of large-scale SLP vari-
137 ability, which emerge objectively from this analysis, are found to be related to coherent
138 sea-ice reemergence events in geographically distinct regions, and suggest an SLP–sea-ice
139 reemergence mechanism.

140 This paper is organized as follows: In section 2, we summarize the coupled NLSA algo-
141 rithm. In section 3, we describe the CCSM3, HadISST, and ERA-Interim datasets used in
142 this study. In section 4, we study the SIC, SST, and SLP spatiotemporal modes obtained
143 via coupled NLSA. In section 5, we examine the regional and temporal characteristics of
144 sea-ice reemergence, and in section 6, we investigate oceanic and atmospheric reemergence
145 mechanisms. We conclude in section 7. Movies, illustrating the spatiotemporal evolution of
146 NLSA modes, are available as online supplementary material.

147 **2. Coupled NLSA methodology**

148 In this study, we apply the coupled NLSA approach, as developed in Bushuk et al. (2014),
149 to Arctic SIC, SST, and SLP. This technique is an extension of the recently developed NLSA
150 algorithm (Giannakis and Majda 2012b, 2013), and provides a scale-invariant approach for
151 multivariate time series analysis. Unlike other multivariate data analysis approaches, coupled
152 NLSA does not require initial normalization of the input fields to unit variance. Rather,
153 the coupled NLSA algorithm implicitly selects the variance ratio between different physical
154 fields, without requiring a choice of normalization by the user. Here, we briefly summarize
155 the method and refer the reader to the more thorough description of Bushuk et al. (2014).
156 Figure 2 is a schematic that summarizes the flow of data in the coupled NLSA algorithm.

157 Let x_t^{SIC} , x_t^{SST} , and x_t^{SLP} be time series for SIC, SST, and SLP, respectively, each sampled

158 uniformly at time step δt , with s time samples. The dimensions of x_t^{SIC} , x_t^{SST} , and x_t^{SLP}
159 are d_{SIC} , d_{SST} , and d_{SLP} , respectively, which are the number of spatial gridpoints for each
160 variable. First, we choose a time lag window $\Delta t = q\delta t$, and time-lag embed our data into the
161 higher dimensional spaces $\mathbb{R}^{d_{\text{SIC}}q}$, $\mathbb{R}^{d_{\text{SST}}q}$, and $\mathbb{R}^{d_{\text{SLP}}q}$. Time-lagged embedding is performed
162 via the delay-coordinate mappings

$$\begin{aligned} x_t^{\text{SIC}} &\mapsto X_t^{\text{SIC}} = (x_t^{\text{SIC}}, x_{t-\delta t}^{\text{SIC}}, \dots, x_{t-(q-1)\delta t}^{\text{SIC}}), \\ x_t^{\text{SST}} &\mapsto X_t^{\text{SST}} = (x_t^{\text{SST}}, x_{t-\delta t}^{\text{SST}}, \dots, x_{t-(q-1)\delta t}^{\text{SST}}), \\ x_t^{\text{SLP}} &\mapsto X_t^{\text{SLP}} = (x_t^{\text{SLP}}, x_{t-\delta t}^{\text{SLP}}, \dots, x_{t-(q-1)\delta t}^{\text{SLP}}). \end{aligned}$$

163 The coupled NLSA approach uses these time-lagged embedded data to construct a set of
164 orthonormal basis functions on the nonlinear data manifold. These basis functions are
165 eigenfunctions of a discrete Laplacian operator, and are computed using a kernel (similarity)
166 function defined through the physical variables of interest, as determined by the user of the
167 algorithm. The kernel and corresponding Laplacian eigenfunctions can be thought of as
168 nonlinear analogs of the covariance matrix and corresponding PCs of SSA, respectively. In
169 this work, the kernel function, K , is an exponentially decaying similarity function constructed
170 using SIC, SST, and SLP, viz.

$$K_{ij} = \exp \left(-\frac{\|X_i^{\text{SIC}} - X_j^{\text{SIC}}\|^2}{\epsilon \|\xi_i^{\text{SIC}}\| \|\xi_j^{\text{SIC}}\|} - \frac{\|X_i^{\text{SST}} - X_j^{\text{SST}}\|^2}{\epsilon \|\xi_i^{\text{SST}}\| \|\xi_j^{\text{SST}}\|} - \frac{\|X_i^{\text{SLP}} - X_j^{\text{SLP}}\|^2}{\epsilon \|\xi_i^{\text{SLP}}\| \|\xi_j^{\text{SLP}}\|} \right),$$

171 where $i, j \in [q + 1, q + 2, \dots, s]$. Here, ϵ is a scale parameter controlling the width of
172 the Gaussian, and $\xi_i^k = X_i^k - X_{i-1}^k$ is the phase space velocity of the k^{th} variable. Note
173 that because of the division by $\|\xi_i^k\|$, the argument of the exponential is unit-independent,
174 allowing for a natural comparison of the different variables in the system. Performing an
175 appropriate normalization, we convert K to a Laplacian matrix, L , and solve the eigenvalue
176 problem

$$L\phi_i = \lambda_i\phi_i.$$

177 This yields a set of discrete Laplacian eigenfunctions $\{\phi_1, \phi_2, \dots, \phi_{s-q}\}$, each of which is a
 178 temporal pattern of length $s - q$. By virtue of the delay-coordinate mapping of the data,
 179 these patterns are conditioned to reveal intrinsic dynamical time scales in the data, such
 180 as those associated with quasi-periodic orbits (Berry et al. 2013). In practice only $l \ll s$
 181 of these eigenfunctions are used and need to be computed. The eigenfunctions are used as
 182 a temporal filter for the data, analogous to Fourier modes, but intrinsic to the dynamical
 183 system generating the data.

184 Let Φ_l be the matrix whose columns consist of the leading l eigenfunctions. Let $X^k : \mathbb{R}^{s-q} \mapsto \mathbb{R}^{qd_k}$ be the lag-embedded data matrix for the k^{th} variable:

$$X^k = \begin{bmatrix} X_{q+1}^k & X_{q+2}^k & \dots & X_s^k \end{bmatrix}.$$

186 Projecting X^k onto the leading l Laplacian eigenfunctions, we construct linear maps $A_l^k : \mathbb{R}^l \mapsto \mathbb{R}^{qd_k}$, given by

$$A_l^k = X^k \mu \Phi_l. \tag{1}$$

188 Here $\vec{\mu}$ is the stationary distribution of the Markov chain corresponding to K , and μ is a
 189 diagonal matrix with $\vec{\mu}$ along the diagonal. Note that the variables used to construct the
 190 eigenfunctions do not necessarily need to coincide with the variables for which we compute
 191 the A_l^k operators. For example, we can use the SIC–SST–SLP eigenfunctions to filter any
 192 other variable of interest in our system.

193 Singular value decomposition (SVD) of the operator for the k^{th} variable, A_l^k , yields a set
 194 of spatiotemporal modes $\{u_n^k\}$ of dimension qd_k , analogous to EEOFs, and a corresponding
 195 set of length l vectors, $\{V_n^k\}$. These $\{V_n^k\}$ are the expansion coefficients in eigenfunction
 196 basis. Expanding using the first l eigenfunctions, we recover a set of temporal modes $\{v_n^k\}$
 197 of length $s - q$, where $v_n^k = \Phi_l V_n^k$. These modes, indexed by n , are ordered by decreasing
 198 singular value. Forming products $u_n^k \sigma_n^k (v_n^k)^T$ and projecting from lagged embedding space
 199 to physical space using the standard approach (Ghil et al. 2002), we obtain reconstructed
 200 fields $\tilde{u}_n^k(t)$.

3. Dataset description

a. CCSM3 model output

This study analyzes model output from a 900-yr equilibrated control integration (model run b30.004) of CCSM3 (Collins et al. 2006). This data was downloaded from the Earth System Grid website. We use monthly averaged data for SIC, SST, and SLP, which come from the Community Sea Ice Model (CSIM, Holland et al. 2006), the Parallel Ocean Program (POP, Smith and Gent 2004), and the Community Atmosphere Model version 3 (CAM3, Collins et al. 2004), respectively. The model uses a T42 spectral truncation for the atmospheric grid (roughly $2.8^\circ \times 2.8^\circ$), and the ocean and sea-ice variables are defined on the same grid, of 1° nominal resolution. This study focuses on a pan-Arctic domain, which we define as all gridpoints north of 45°N . Note that the seasonal cycle has not been removed from this dataset. This is crucial for capturing intermittent patterns associated with reemergence. In particular, intermittent modes, described ahead in section 4, are not recoverable in datasets that have been deseasonalized (Giannakis and Majda 2013). As will be shown ahead in section 5, these modes are essential in low dimensional descriptions of sea-ice reemergence.

The spatial dimensions (number of spatial gridpoints) of these datasets are $d_{\text{SIC}} = d_{\text{SST}} = 13,202$ and $d_{\text{SLP}} = 2,048$. Using a two-year embedding window with $q = 24$ (Giannakis and Majda 2012b; Bushuk et al. 2014), this yields lagged embedding dimensions (the product of the number of spatial gridpoints and the embedding window) of $qd_{\text{SIC}} = qd_{\text{SST}} = 316,848$ and $qd_{\text{SLP}} = 49,152$. These data are monthly averaged, and consist of $s = 10,800$ time samples for the 900-yr simulation period. The value $\Delta t = 24$ months was used as the time lag because this embedding window is longer than the seasonal cycle, which is a primary source of non-Markovianity in this dataset. A number of different embedding windows were tested, yielding qualitatively similar results for $\Delta t \geq 12$ months, and qualitatively different results for $\Delta t < 12$ months.

226 *b. HadISST observations*

227 We also analyze the HadISST dataset (Rayner et al. 2003), which consists of monthly
228 averaged SIC and SST data on a 1° latitude-longitude grid. The spatial dimension of the
229 Arctic domain is $d_{\text{SIC}} = d_{\text{SST}} = 9,453$. As with the CCSM3 data, we use an embedding
230 window of $\Delta t = 24$ months, which yields lagged-embedding dimensions of $qd_{\text{SIC}} = qd_{\text{SST}} =$
231 $226,872$. In this study we use the satellite era data from January 1979–August 2013. Note
232 that all ice-covered gridpoints in the HadISST dataset were assigned an SST value of -1.8°C ,
233 the freezing point of salt water at a salinity of 35 parts per thousand. Also, the trend in
234 the dataset was removed by computing a long-term linear trend for each month of the year,
235 and removing the respective linear trend from each month. The seasonal cycle has not been
236 removed from this dataset.

237 *c. ERA-Interim reanalysis data*

238 Finally, we also study monthly-averaged SLP data from the European Centre for Medium-
239 Range Weather Forecasts (ECMWF) Interim Reanalysis project (ERA-Interim, Dee et al.
240 2011). These data are defined on a 0.75° latitude–longitude grid, of considerably higher
241 resolution than the CCSM3 SLP data. The spatial dimension of the Arctic domain is $d_{\text{SLP}} =$
242 $29,280$, corresponding to a lagged-embedding dimension of $qd_{\text{SLP}} = 702,720$. These data have
243 been detrended by subtracting the monthly trend from each month, but the seasonal cycle
244 has not been subtracted.

245 **4. Coupled SIC-SST-SLP spatiotemporal modes of Arc-**
246 **tic variability**

247 We utilize the coupled NLSA algorithm outlined in section 2 to study the spatiotemporal
248 evolution of (i) SIC, SST, and SLP in CCSM3; and (ii) SIC and SST from HadISST, and SLP

249 from ERA-Interim. Hereafter, we refer to the joint HadISST and ERA-Interim datasets as
 250 observations. For both the model and observational data, we use a lagged-embedding window
 251 of $\Delta t = 24$ months.

252 *a. CCSM3 Modes*

253 We choose ϵ , the Gaussian locality parameter, as $\epsilon = 0.90$. Using the spectral entropy
 254 criterion of Giannakis and Majda (2012a, 2013), we select a truncation level of $l = 27$
 255 eigenfunctions, and express the data matrices X^{SIC} , X^{SST} , and X^{SLP} in this basis. SVD of
 256 the resulting operators (see eq. 1) yields a set of spatiotemporal patterns, $\{u_n^{\text{SIC}}\}$, $\{u_n^{\text{SST}}\}$,
 257 $\{u_n^{\text{SLP}}\}$, and a set of temporal patterns, $\{v_n^{\text{SIC}}\}$, $\{v_n^{\text{SST}}\}$, $\{v_n^{\text{SLP}}\}$, for each variable. The modes
 258 are ordered by decreasing singular value. In general, the temporal patterns for different
 259 variables need not be related. However, by virtue of the relatively low-dimensionality of the
 260 eigenfunction basis relative to the original temporal dimension ($l = 27 \ll s = 10,800$), and
 261 the fact that the eigenfunctions incorporate information from all three variables, we find
 262 strong correlations between the temporal patterns of different variables.

263 1) TEMPORAL MODES

264 Figures 3, 4, and 5 show selected temporal patterns for SIC, SST, and SLP, respectively.
 265 For each variable, we observe three distinct types of temporal modes: periodic, low-frequency,
 266 and intermittent modes, indicated by P , L , and I in the figures.

267 The periodic temporal modes closely resemble sinusoids, with frequencies given by in-
 268 teger multiples of 1 yr^{-1} . These modes appear as doubly degenerate pairs, with a phase
 269 offset of $\pi/2$. The leading periodic modes, representing the annual and semiannual cycles,
 270 capture more variance than the low-frequency and intermittent modes of the system. Higher
 271 harmonic periodic modes are found later in the mode spectrum. The low-frequency modes
 272 are characterized by significant interannual variability, and have a typical decorrelation time

273 of approximately 3 years. These modes carry significant spectral power at frequencies below
274 1 yr^{-1} , and exhibit a sharp decline in spectral power at frequencies above this.

275 The intermittent modes are characterized by periods of intense activity followed by pe-
276 riods of quiescence. Each intermittent mode has a base frequency of oscillation, and a
277 broadband peak in spectral power centered upon this frequency. These modes carry lower
278 variance than their periodic and low-frequency counterparts, yet have potentially high dy-
279 namical significance. For example, annual and semiannual intermittent modes are crucial
280 components in low-dimensional descriptions of sea-ice reemergence phenomena (Bushuk et al.
281 2014). Note that the leading low-frequency and intermittent modes are insensitive to trun-
282 cation level, whereas increasing l will eventually disrupt the temporal character of some
283 intermittent modes.

284 Intermittent modes closely resemble a periodic signal modulated by a low-frequency enve-
285 lope. We find that nearly all intermittent modes can be directly associated with a particular
286 low-frequency mode, which provides this modulating envelope (Bushuk et al. 2014). To de-
287 termine this association we compare the envelope function of the intermittent modes to the
288 low-frequency modes. We find the envelope function via the Hilbert transform (von Storch
289 and Zwiers 1999). Let $I(t)$ be a given intermittent mode and let $H(I)(t)$ be the Hilbert
290 transform of I . Then the envelope function, $e(t)$, is given by $e(t) = \sqrt{I(t)^2 + H(I)(t)^2}$.
291 Next, we determine which low-frequency mode provides this modulating envelope by per-
292 forming a correlation between $e(t)$ and $|L(t)|$, where $L(t)$ is a low-frequency mode. Fig. 6
293 shows these correlation values for intermittent and low-frequency modes of each variable, for
294 both the model and observations. Note that the low-frequency-intermittent mode associa-
295 tion is quite clear for most variables, except for the observational SLP, whose intermittent
296 envelopes generally correlate weakly with the low-frequency modes.

297 As a comparison, we also performed SSA on the concatenated and unit-variance normal-
298 ized SIC-SST-SLP dataset. Similar to the findings of Bushuk et al. (2014), SSA produces
299 periodic modes, many low-frequency modes, and some modes that loosely resemble the in-

300 intermittent modes of NLSA, with a spectral maximum at a certain base frequency. We find
301 that the SSA modes do not share the same intermittent–low-frequency mode relationships
302 as the NLSA modes. These relationships will be important for explaining reemergence, as
303 they reflect the interaction of large-scale low-frequency modes of variability with the familiar
304 annual and semiannual cycles in the climate system.

305 2) SIC SPATIOTEMPORAL PATTERNS

306 Figure 7 shows spatial patterns of selected modes at a snapshot in time. Movies 1 and 2,
307 in the online supplementary material, show the spatiotemporal evolution of these modes and
308 others. Below, we describe the prominent features of the spatiotemporal modes recovered
309 for SIC, SST, and SLP.

310 The annual periodic SIC modes, $\{P_1^{\text{SIC}}, P_2^{\text{SIC}}\}$ (Fig. 7a), have spatially uniform anomalies
311 throughout most of the Arctic, except at high-latitude gridpoints where there is year-round
312 ice coverage, and in the marginal ice zones, where the anomalies are slightly weaker. These
313 anomalies reach their maximum and minimum values in March and September, respectively.
314 The higher-frequency periodic modes have increasingly finer spatial structure, and capture
315 a decreasing portion of the variance.

316 The low-frequency modes closely resemble the leading EOFs of Arctic SIC in the CCSM3
317 model. L_1^{SIC} (Fig. 7d) exhibits anomalies in the Bering, Beaufort, and Labrador Seas, which
318 are out-of-phase with the anomalies of the Barents, Kara, and Greenland Seas. Computing
319 pattern correlations between the q spatial patterns of L_1^{SIC} and the different EOFs of de-
320 seasonalized Arctic SIC, we find a maximum pattern correlation of 0.97 with EOF 1. L_2^{SIC}
321 (Fig. 7g) has strong anomalies in the Bering and Labrador Seas, which are out-of-phase
322 with one another. It also has weaker anomalies in the Sea of Okhotsk, Barents and Kara
323 seas which are in-phase with the Bering Sea anomalies. This mode has a maximum pattern
324 correlation of 0.77 with EOF 3.

325 Each intermittent mode has a natural association with a certain low-frequency mode,

326 which acts as a modulating envelope for the intermittent mode. There is also a clear spatial
 327 connection, as the intermittent modes are active in the same parts of the domain as their
 328 low-frequency counterpart. The annual and semiannual intermittent mode pairs, $\{I_1^{\text{SIC}}, I_2^{\text{SIC}}\}$
 329 and $\{I_7^{\text{SIC}}, I_8^{\text{SIC}}\}$, are associated with L_1^{SIC} (see Fig. 6). These modes pulse with annual
 330 and semiannual frequency, respectively, and exhibit finer spatial structure than L_1^{SIC} . In
 331 regions where L_1^{SIC} has monopole anomalies, these intermittent modes have dipole and tripole
 332 anomalies, respectively. The annual and semiannual intermittent modes, $\{I_3^{\text{SIC}}, I_4^{\text{SIC}}\}$ and
 333 $\{I_9^{\text{SIC}}, I_{10}^{\text{SIC}}, I_{11}^{\text{SIC}}\}$, are associated with L_2^{SIC} , and share similar spatial relationships.

334 3) SST SPATIOTEMPORAL PATTERNS

335 L_1^{SST} (Fig. 7e) has strong anomalies in the Bering Sea that extend southward into the
 336 Northeast Pacific, and anomalies of the opposite sign in the Barents and Kara Seas. There
 337 is also a North Atlantic signal with anomalies in the subpolar gyre region that are in-phase
 338 with the North Pacific anomalies. This mode has a maximum pattern correlation of 0.98
 339 with EOF 1 of Arctic SST from CCSM3. L_2^{SST} (Fig. 7h) exhibits out-of-phase anomalies
 340 between the North Pacific and North Atlantic. The North Atlantic anomalies correspond to
 341 variability in the subpolar gyre, and the North Pacific anomalies are strongest in the Bering
 342 Sea, extending through most of the Pacific portion of the domain. This mode is most similar
 343 to EOF 2, with 0.96 pattern correlation.

344 The intermittent modes associated with L_1^{SST} and L_2^{SST} are $\{I_1^{\text{SST}}, I_2^{\text{SST}}, I_8^{\text{SST}}, I_9^{\text{SST}}\}$ and
 345 $\{I_5^{\text{SST}}, I_6^{\text{SST}}, I_{11}^{\text{SST}}\}$, respectively. As with the SIC modes, these modes are active in the
 346 same parts of the domain as their associated low-frequency mode, and have finer spatial
 347 structure. A primary difference is that these intermittent modes exhibit spatially propagating
 348 anomalies, as compared with their stationary SIC counterparts. This propagation is most
 349 evident in the subpolar gyre region of the North Atlantic.

350 4) SLP SPATIOTEMPORAL PATTERNS

351 L_1^{SLP} (Fig. 7f) has a similar SLP pattern to the AO, with an anomaly centered over the
 352 pole, and anomalies of opposite sign in the North Atlantic and North Pacific basins. The
 353 AO is defined as the leading EOF of SLP north of 20°N . Considering EOFs of CCSM3 SLP
 354 north of 20°N , we find a maximum pattern correlation of 0.98 with EOF 1. In light of this
 355 strong correlation, we call L_1^{SLP} the AO mode. L_2^{SLP} also closely resembles the AO, with a
 356 maximum pattern correlation of 0.98 with EOF 1. However, L_1^{SLP} and L_2^{SLP} have distinct
 357 temporal patterns and are non-degenerate modes.

358 L_3^{SLP} (Fig. 7i) has a strong resemblance to the DA, which consists of opposite-signed SLP
 359 anomalies between the Eastern and Western Arctic. Following Wu et al. (2006), we define the
 360 dipole anomaly as the second leading EOF of winter (October-March) SLP north of 70°N . Let
 361 PC 2 be the PC associated with EOF 2. To determine the corresponding spatial pattern over
 362 the Arctic domain (north of 45°N), we project winter Arctic SLP onto PC 2, and compare
 363 the resulting spatial pattern to L_3^{SLP} . We find a maximum pattern correlation of 0.78, and
 364 lower correlations when other PCs are used. Another possible technique for determining the
 365 Arctic SLP signal of the DA, as performed in Wu et al. (2006), is to perform a conditional
 366 composite, based on the months in which PC 2 is active. This yields a very similar pattern
 367 correlation of 0.77 with L_3^{SLP} . Wu et al. (2006) also perform a conditional composite in
 368 which the influence of the AO is removed via linear regression. We also computed a spatial
 369 pattern using this technique and found a pattern correlation of 0.78 with L_3^{SLP} . Based on
 370 these findings, we refer to L_3^{SLP} as the DA mode.

371 L_1^{SLP} has associated annual and semiannual intermittent modes $\{I_1^{\text{SLP}}, I_2^{\text{SLP}}, I_9^{\text{SLP}}, I_{10}^{\text{SLP}}\}$.
 372 L_3^{SLP} is associated with a pair of annual intermittent modes $\{I_7^{\text{SLP}}, I_8^{\text{SLP}}\}$, but not any semi-
 373 annual intermittent modes.

374 *b. Observational Modes*

375 We compute the coupled NLSA observational modes using a locality parameter of $\epsilon = 1.20$
376 and a truncation level of $l = 21$ eigenfunctions. A primary difference between the observa-
377 tional modes and CCSM3 modes is the variables used for the eigenfunction computation.
378 We find that computing SIC-SST-SLP eigenfunctions from the observational datasets yields
379 temporal modes which are significantly noisier (more high-frequency power) than the corre-
380 sponding modes from CCSM3. This corruption occurs due to the inclusion of the SLP data
381 in the eigenfunction computation. We find that the eigenfunctions are substantially cleaner
382 when computed using SIC and SST, and we use this as the base case for this study. On the
383 other hand, the CCSM3 results are insensitive to the inclusion of SLP, with SIC-SST-SLP
384 and SIC-SST eigenfunctions yielding very similar modes and conclusions regarding sea-ice
385 reemergence. We obtain SLP observational modes by projecting the SLP data onto the
386 SIC-SST eigenfunctions and performing an SVD of the resulting operator. Note that the
387 observational SLP data is roughly 4 times finer spatial resolution than the CCSM3 SLP data.
388 This discrepancy in resolution may explain the corruption in observational modes compared
389 with CCSM3 modes. An NLSA kernel that incorporates an initial spatial smoothing of the
390 input data (making them comparable to the T42 resolution of the CCSM3 data) could al-
391 leviate these issues, but we elected not to carry out these calculations since we are able to
392 identify reemergence families, ahead, using SIC and SST only as inputs to the kernel.

393 The observational temporal modes have a similar character to those obtained from
394 CCSM3. For each variable, we find periodic, low-frequency, and intermittent modes, and in
395 many cases the low-frequency modes act as modulating envelopes for the intermittent modes.
396 The temporal modes for SIC, SST, and SLP are shown in Figs. 1-3 of the supplementary
397 material.

398 Next, we provide a brief description of the spatiotemporal modes that will be discussed
399 later in the paper. Movies 3 and 4 of the supplementary material provide a more revealing
400 spatiotemporal evolution of these modes and others. L_1^{SIC} (Fig. 7j) closely resembles the

401 leading EOF of winter Arctic sea ice reported by Deser et al. (2000). In its positive phase,
 402 L_1^{SIC} has positive sea-ice anomalies in the Labrador and Bering seas and negative anomalies
 403 in the Greenland, Barents-Kara, and Okhotsk Seas. This mode has a maximum pattern
 404 correlation of 0.88 with EOF 1 of Arctic sea ice from HadISST. L_1^{SST} (Fig. 7k) is most
 405 similar to EOF 2 of Arctic SST, with a maximum pattern correlation of 0.70. In positive
 406 phase, this mode has positive anomalies in the Labrador Sea and subpolar gyre region,
 407 negative anomalies in the Barents-Kara Seas and positive anomalies in the Bering Sea. L_1^{SLP}
 408 (Fig. 7l) strongly resembles the annular structure of the AO. Computing EOFs of ERA-
 409 Interim SLP north of 20°N, we find a maximum pattern correlation of 0.97 with EOF 1, the
 410 AO pattern. Similar to the CCSM3 results, the intermittent modes are generally associated
 411 with a low-frequency mode, are active in the same parts of the domain as this low-frequency
 412 mode, and display finer spatial structure.

413 One feature which is conspicuously absent from the observational SLP modes is a DA-
 414 like mode. Other fields, such as 850mb geopotential height and surface winds, and smaller
 415 domains were tested, but a low-frequency DA mode analogous to the CCSM3 results was
 416 not found. Certain modes obtained were quite transient, and resembled the DA pattern at
 417 certain snapshots in time, but not persistently.

418 *c. Interpretation of low-frequency SLP modes*

419 The low-frequency SLP modes have spatial patterns that closely resemble the famil-
 420 iar spatial patterns obtained via EOF analysis. However, their temporal behavior differs
 421 substantially. The low-frequency NLSA temporal modes have significant one-year auto-
 422 correlation and carry most of their power at frequencies below 1 yr⁻¹. This lies in sharp
 423 contrast to the PCs obtained via EOF analysis, which have a nearly white power spectrum
 424 and decorrelate very rapidly, losing all memory after 1-2 months. Despite these extremely
 425 different temporal characteristics, there is natural connection between the two: the low-
 426 frequency NLSA modes closely resemble a low-pass filtered version of the noisy PCs from

427 EOF analysis.

428 This is illustrated in Fig. 8, which shows temporal behavior for L_1^{SLP} , the leading low-
429 frequency NLSA mode from CCSM3, PC_1^{SLP} , the principal component corresponding to the
430 leading EOF of SLP, and $\langle \text{PC}_1^{\text{SLP}} \rangle$, a low-pass filtered version of PC_1^{SLP} , computed by taking
431 a 24 month running mean. L_1^{SLP} has a relatively low correlation of 0.31 with PC_1^{SLP} , but
432 a significantly higher correlation of 0.80 with the low-pass filtered PC, $\langle \text{PC}_1^{\text{SLP}} \rangle$. L_1^{SLP} and
433 $\langle \text{PC}_1^{\text{SLP}} \rangle$ share qualitatively similar autocorrelation functions and power spectra, which are
434 very different from the rapidly decaying autocorrelation and nearly white power spectrum
435 of PC_1^{SLP} . These results suggest a natural interpretation of the low-frequency NLSA modes
436 as low-pass filtered versions of the PCs from EOF analysis, which emphasize variability on
437 interannual to decadal timescales and filter out higher-frequency variability. It is important
438 to note that the low-frequency NLSA modes have weak sensitivity to the lag-embedding
439 window Δt (as long as $\Delta t \geq 12$; see section 3). Also, a univariate NLSA analysis with only
440 SLP was performed, and similar low-frequency modes were recovered. This suggests that
441 these low-frequency patterns describe an intrinsic component of SLP variability, which in
442 this case can be reproduced by an ad-hoc running averaging of the data.

443 The observational SLP modes also display a similar correspondence, with a correlation
444 of 0.83 between $\langle \text{PC}_1^{\text{SLP}} \rangle$ and L_1^{SLP} . This high correlation indicates that the SIC-SST eigen-
445 functions used for the observational data are able to capture important variability in the
446 raw SLP data.

447 **5. Arctic sea-ice reemergence in models and observa-** 448 **tions**

449 Sea-ice reemergence is a time-lagged correlation phenomenon. SIC anomalies decorrelate
450 over a 3-6 month timescale, however, at some time lag in the future, an increase in correlation
451 occurs. Sea-ice reemergence is observed in two forms: a spring-fall reemergence, in which

452 spring anomalies are reproduced the following fall, and a fall-spring reemergence, in which
453 fall anomalies are reproduced the following spring. Both forms are observed in CCSM3 model
454 output and HadISST observations, with the spring-fall reemergence being the significantly
455 stronger signal in both cases.

456 We study sea-ice reemergence via the time-lagged pattern correlation methodology of
457 Bushuk et al. (2014). For each month of the year, pattern correlations are computed between
458 the SIC anomaly field of the given month and the SIC field at lags of 0 to 23 months into
459 the future. This is done for all (month, month+lag) pairs in the time series, and we report
460 the average of these correlation values. Note that the pattern correlations are performed on
461 anomalies from the seasonal cycle, are area-weighted, and are uncentered (global mean has
462 not been subtracted from the anomaly field). This differs from the approach of Blanchard-
463 Wrigglesworth et al. (2011), where the lagged correlations were performed using a time
464 series of total sea-ice area. Performing correlations using the full SIC field, as opposed to its
465 total area, allows for inclusion of the spatial distribution of sea ice. The pattern correlation
466 approach is able to detect opposite-signed anomaly features, such as sea-ice dipoles, which
467 would be integrated away in the total area approach. It also enforces a notion of locality,
468 since anomalies must be spatially coincident in order to yield a significant pattern correlation.
469 This ensures that a reported sea-ice reemergence signal represents recurrent anomalies at the
470 same spatial location.

471 In this paper, we focus on the regions defined in Fig. 1: a pan-Arctic domain ($0^\circ - 360^\circ$
472 and $45^\circ\text{N} - 90^\circ\text{N}$), the Barents and Kara Seas ($30^\circ\text{E} - 90^\circ\text{E}$ and $65^\circ\text{N} - 80^\circ\text{N}$), the Labrador
473 Sea and Baffin Bay ($70^\circ\text{W} - 40^\circ\text{W}$ and $45^\circ\text{N} - 80^\circ\text{N}$), the Greenland Sea ($40^\circ\text{W} - 0^\circ\text{E}$ and
474 $55^\circ\text{N} - 80^\circ\text{N}$), the Bering Sea ($165^\circ\text{E} - 160^\circ\text{W}$ and $55^\circ\text{N} - 65^\circ\text{N}$), and the Sea of Okhotsk
475 ($135^\circ\text{E} - 165^\circ\text{E}$ and $45^\circ\text{N} - 65^\circ\text{N}$).

477 We begin with a regional study of sea-ice reemergence using raw SIC data from HadISST
478 observations and CCSM3 output, the results of which are shown in Fig. 9. This figure shows
479 time-lagged pattern correlations, computed for all initial months and lags of 0 to 23 months.
480 All correlations plotted in color are greater than 0.1 and are significant at the 95% level,
481 based on a t -distribution statistic, which tests for the statistical significance of the time-mean
482 pattern correlation values against a null hypothesis that there is no correlation.

483 Over a pan-Arctic domain, in both the model and observations, we observe a clear “sum-
484 mer limb” of positive correlations corresponding to sea-ice anomalies that originate in the
485 melt season (March-August) and reemerge in the growth season (Fig. 9a,b). The “win-
486 ter limb” of fall-spring reemergence, corresponding to anomalies originating in September-
487 February, is weak over the Arctic domain, except for a small hint of the limb in the CCSM3
488 data. An interesting consequence of the time-lagged pattern correlation approach is the
489 striking similarity of pan-Arctic lagged correlations in CCSM3 and observations. This lies in
490 contrast to the total area lagged correlation methodology of previous studies, which reveal
491 a clearly enhanced reemergence signal in the model relative to observations (Blanchard-
492 Wrigglesworth et al. 2011; Day et al. 2014). This indicates that, despite differences in
493 memory of total sea-ice area anomalies, the model and observations are quite similar in their
494 memory of sea-ice spatial patterns.

495 The pan-Arctic reemergence signal is similar in the model and observations, however a
496 regional analysis reveals significant differences between the two. Both CCSM3 and HadISST
497 have strong summer limb signals in the Barents-Kara domain (Fig. 9g,h) and the Greenland
498 Sea (Fig. 9k,l). The CCSM3 data also exhibits a winter limb in the Barents-Kara domain,
499 which is not significant in observations. A striking difference is found in the Labrador Sea,
500 with a strong summer limb and a significant winter limb in observations, neither of which
501 are found in the model (Fig. 9i,j). Conversely, the strong summer limbs in the Bering and
502 Okhotsk Seas found in the model data are absent in the observations (Fig. 9c,d,e,f). Note

503 that the winter limb signal in the Bering and Okhotsk Seas should not be over-interpreted,
 504 as these domains are essentially sea-ice free during the summer and early fall. Therefore, the
 505 North Pacific winter limb lagged correlations are performed using an extremely low-variance
 506 signal, and are not robust.

507 *b. Sea-ice reemergence revealed via coupled NLSA*

508 Given the non-trivial lagged correlation structures in the CCSM3 and HadISST sea-ice
 509 datasets, we seek a low-dimensional representation of sea-ice reemergence via the coupled
 510 NLSA modes obtained in Section 4. We aim to answer two main questions: (1) Can the
 511 reemergence signal of the raw data be efficiently reproduced by low-dimensional families of
 512 modes? (2) Can these mode families reveal possible mechanisms for Arctic sea-ice reemer-
 513 gence? To answer the former, we perform time-lagged pattern correlations using small
 514 subsets of reconstructed spatiotemporal fields from coupled NLSA. Our approach here is to
 515 first construct families of SIC modes, and then to augment these families with SST and SLP
 516 modes, based on correlations.

517 1) CCSM3 REEMERGENCE FAMILIES

518 Based on the associations between low-frequency and intermittent modes identified in
 519 section 4a.1, we construct two families of SIC modes, each consisting of a low-frequency
 520 mode and annual and semiannual intermittent modes. These families, which we refer to as
 521 \mathcal{F}_1^M and \mathcal{F}_2^M , are able to qualitatively reproduce the reemergence signal of the raw data. They
 522 are given by $\mathcal{F}_1^M = \{L_1^{\text{SIC}}, I_1^{\text{SIC}}, I_2^{\text{SIC}}, I_7^{\text{SIC}}, I_8^{\text{SIC}}\}$ and $\mathcal{F}_2^M = \{L_2^{\text{SIC}}, I_3^{\text{SIC}}, I_4^{\text{SIC}}, I_9^{\text{SIC}}, I_{10}^{\text{SIC}}, I_{11}^{\text{SIC}}\}$.
 523 Here, the M superscript indicates that these families come from model output. Each family
 524 is particularly active in the Barents-Kara, Bering, and Labrador Seas, but shares different
 525 phase relationships between the different regions. Within each family, the low-frequency and
 526 intermittent modes are closely related, in the sense that the low-frequency mode provides the

527 modulating envelope for the intermittent modes. This means that all modes in a given family
 528 tend to be active or inactive at the same times. Note that similar envelope associations were
 529 observed in the reemergence families identified in Bushuk et al. (2014), suggesting that this
 530 approach may be useful in a broader context. Many other mode subsets were tested, but were
 531 unable to reproduce the lagged correlation structure as effectively as these families, likely
 532 because they lack the envelope relationships that characterize the families. Moreover, \mathcal{F}_1^M
 533 and \mathcal{F}_2^M appear to be the minimal mode subsets, as smaller sets are unable to qualitatively
 534 reproduce the reemergence signal.

535 In Fig. 10d, we show time-lagged pattern correlations computed over the Arctic domain
 536 using NLSA family \mathcal{F}_1^M . Comparing with the time-lagged pattern correlation structure of the
 537 raw data, shown in Fig. 10a, we observe qualitatively similar features. The \mathcal{F}_1^M correlations
 538 have a clear summer limb structure, with correlations that decay to near zero over the
 539 summer months and reemerge the following fall. They also have a slightly weaker winter
 540 limb, which may correspond to the weaker fall-spring reemergence seen in the raw data. The
 541 \mathcal{F}_1^M correlations are substantially higher than the raw data correlations because the family's
 542 activity is primarily governed by L_1^{SIC} , which has a decorrelation time of 3 years.

543 This NLSA family has a qualitatively similar correlation structure to the raw data, yet it
 544 is natural to ask whether this family is capturing the portion of the signal responsible for the
 545 summer limb in the raw data. As a method for addressing this question, we compute time-
 546 lagged cross correlations between the raw data and the NLSA subspaces, shown in Fig. 10b
 547 and 10c. To explain panels b and c, we introduce $LC(A, B)$, a function that computes time-
 548 lagged pattern correlations, with the dataset B lagging A . Using this notation, Fig. 10a
 549 shows $LC(\text{Raw}, \text{Raw})$ and Fig. 10d shows $LC(\mathcal{F}_1^M, \mathcal{F}_1^M)$. In Fig. 10b and 10c, we plot
 550 $LC(\text{Raw}, \mathcal{F}_1^M)$ and $LC(\mathcal{F}_1^M, \text{Raw})$, respectively.

551 If the reemergence signal of \mathcal{F}_1^M is not representative of the signal in the raw data, one
 552 would expect these cross correlations to be small. However, we observe strong summer limbs
 553 in panels 10b and 10c, similar to the correlation structure of the raw data. The fact that

554 these panels are similar to panel 10a, indicates that family \mathcal{F}_1^M is capturing the portion of
 555 the data responsible for the sea-ice reemergence signal.

556 In Fig. 10e-h, we plot the same quantities as Fig. 10a-d, but for Family \mathcal{F}_2^M . $LC(\mathcal{F}_2^M, \mathcal{F}_2^M)$
 557 also has a strong summer limb and a weaker winter limb, but each of these limbs is weaker
 558 than their respective counterparts in $LC(\mathcal{F}_1^M, \mathcal{F}_1^M)$. Also, $LC(\text{Raw}, \mathcal{F}_2^M)$ and $LC(\mathcal{F}_2^M, \text{Raw})$,
 559 plotted in Fig. 10f and 10g, shows partial summer limbs, but these correlations are weaker
 560 than the reemergence signal of the raw data. This indicates that family \mathcal{F}_2^M is capturing
 561 some of the reemergence signal, but not as significant a portion as family \mathcal{F}_1^M .

562 2) HADISST REEMERGENCE FAMILIES

563 The observational modes also admit a mode family which is able to reproduce the reemer-
 564 gence signal of the raw HadISST data. This family is given by $\mathcal{F}_1^O = \{L_1^{\text{SIC}}, I_1^{\text{SIC}}, I_2^{\text{SIC}}, I_5^{\text{SIC}}, I_6^{\text{SIC}}\}$,
 565 where the O indicates observational data. There is no clear second family which has non-
 566 trivial cross-correlations with the raw observational data. In Fig. 11 we plot time-lagged
 567 cross correlations for \mathcal{F}_1^O . $LC(\mathcal{F}_1^O, \mathcal{F}_1^O)$ has a clear summer limb and a weaker winter limb.
 568 We also find a strong summer limb structure in $LC(\text{Raw}, \mathcal{F}_1^O)$ and $LC(\mathcal{F}_1^O, \text{Raw})$, except for
 569 a small gap in the limb for anomalies beginning in July. This indicates that the family \mathcal{F}_1^O
 570 is capturing a substantial portion of the reemergence signal in the raw data.

571 c. Variance explained by reemergence families

572 Another way to test the effectiveness of the families in capturing the reemergence signal is
 573 to directly subtract the families from the raw sea-ice data, and compute time-lagged pattern
 574 correlations on the resulting dataset. Fig. 12c shows $LC(\text{Raw} - \mathcal{F}_1^M - \mathcal{F}_2^M, \text{Raw} - \mathcal{F}_1^M - \mathcal{F}_2^M)$,
 575 and Fig. 12d shows $LC(\text{Raw} - \mathcal{F}_1^O, \text{Raw} - \mathcal{F}_1^O)$. Each of these has a clearly reduced summer
 576 limb relative to $LC(\text{Raw}, \text{Raw})$, which are shown in Fig. 12a for CCSM3 and Fig. 12b
 577 for HadISST. This demonstrates that the reemergence families are capturing a substantial

578 portion of the reemergence signal. In terms of total sea-ice area anomalies, family \mathcal{F}_1^M
579 explains 41%, 25%, and 8% of the variance in the Bering, Barents-Kara, and Labrador Seas,
580 respectively. Similarly, \mathcal{F}_2^M explains 18%, 1%, and 14% of the variance, and \mathcal{F}_1^O explains
581 7%, 30%, and 18% of the variance, in these respective regions.

582 The variance explained by these families is lower if one considers the full (non-integrated)
583 sea-ice anomaly field. Over the full Arctic domain family \mathcal{F}_1^M explains 5% of the variance,
584 \mathcal{F}_2^M explains 3% and \mathcal{F}_1^O explains 7%. While these values seem somewhat low, it is inter-
585 esting to note that the leading two EOFs from CCSM3 capture 7% and 6% of the variance,
586 respectively. These values are lower than those typically reported in EOF studies for three
587 reasons: (1) the spatial domain is large; (2) there has been no temporal smoothing or averag-
588 ing performed; and (3) the spatial resolution is relatively fine. For example, the leading EOF
589 of Deser et al. (2000) captures 35% of the sea-ice variance in the Arctic, but this is based on a
590 time series of winter mean sea-ice anomalies. This temporal averaging substantially smooths
591 the data, and the leading EOF captures variance more efficiently in this time-filtered dataset.
592 By contrast, the leading 10 EOFs of CCSM3 Arctic sea ice capture 38% of the variance.

593 The comparison with SSA, a variance greedy algorithm, is also illuminating. The leading
594 two SSA modes capture 2.5% and 2% of the variance, respectively, and the leading 10
595 non-periodic SSA modes capture 14% of the variance. By comparison, the leading 10 non-
596 periodic NLSA modes capture 10% of the variance, which is modestly less than SSA. The
597 main reason for this discrepancy is that the intermittent modes of NLSA carry less variance
598 than low-frequency modes. Despite being low-variance, these intermittent modes are crucial
599 components of the reemergence families and illustrate an important point: low-variance
600 modes can play an important role in explaining dynamical phenomena.

601 *d. Temporal variability of sea-ice reemergence*

602 To this point, all reported lagged correlations have been time-mean values, computed over
603 the full time series. Next, we consider the time-dependent aspects of sea-ice reemergence.

604 Fig. 12e shows lagged correlations of the raw CCSM3 sea-ice data, conditional on the low-
 605 frequency modes of \mathcal{F}_1^M or \mathcal{F}_2^M , L_1^{SIC} and L_2^{SIC} , being active. Specifically, we condition on
 606 all times for which $|L_1^{\text{SIC}}(t)| > 2$ or $|L_2^{\text{SIC}}(t)| > 2$ (which corresponds to 11% of the data).
 607 Similarly, Fig. 12f shows lagged correlations of the raw HadISST data conditional on the
 608 low-frequency mode of \mathcal{F}_1^O being active ($|L_1^{\text{SIC}}(t)| > 1.5$, which corresponds to 14% of the
 609 data). We observe a clearly enhanced reemergence signal (both summer and winter limbs)
 610 during times when these modes are active. Figs. 12g and 12h show lagged correlations
 611 conditional on these modes being inactive ($|L_1^{\text{SIC}}(t)| < 1$ and $|L_2^{\text{SIC}}(t)| < 1$ for CCSM3 and
 612 $|L_1^{\text{SIC}}(t)| < 1$ for HadISST). This corresponds to 45% and 59% of the data, respectively. In
 613 both cases, particularly with CCSM3, we observe a diminished reemergence signal. These
 614 results indicate that reemergence events have significant temporal variability, characterized
 615 by regimes of quiescence and other regimes of intense activity. Another notable feature is the
 616 robust initial decay of correlation for lags of 0–3 months. The most significant differences
 617 between Figs. 12e,f and Figs. 12g,h occur at lags greater than 3 months, indicating that
 618 reemergence events display more temporal variability than the initial decay of persistence.
 619 Note that due to the shortness of observational record, the conditional correlations from
 620 HadISST are less robust than those from CCSM3.

621 In CCSM3, about half of the record is characterized by a very weak reemergence signal
 622 (Fig. 12g), whereas other times exhibit strong reemergence (Fig. 12e). This may have impor-
 623 tant implications for sea-ice predictability, since predictability resulting from reemergence
 624 will have a strong temporal dependence, dependent on the strength of the reemergence sig-
 625 nal at a given time. The results here also demonstrate the efficacy of certain low-frequency
 626 NLSA modes as predictors for the strength of reemergence events. Therefore, these modes
 627 could be a valuable addition to statistical sea-ice forecast models.

628 As another method to test the temporal variability of reemergence events, we measure
 629 the strength of the reemergence signal as a function of time. We define the reemergence
 630 strength as the sum of correlation values along the summer limb, compute this quantity for

631 each year of the time series, and create a probability density function (PDF). The PDF (not
632 shown here) is close to Gaussian, with a slight skew towards large reemergence events. If we
633 let μ be the mean of the PDF, we find that 23% of reemergence events are less than 0.5μ and
634 23% of events are greater than 1.5μ . This spread in event distribution demonstrates that
635 reemergence strength fluctuates strongly in time.

636 This temporal characterization of Arctic reemergence events is a new result of this study,
637 which was inaccessible in previous studies of reemergence based on time-lagged total area
638 correlations. In the time-lagged pattern correlation methodology, correlations are performed
639 space, rather than time, which allows for the temporal variations of these correlations to
640 be studied. The mode families also allow for an investigation of the temporal variability of
641 reemergence events and mechanisms, and this will be returned to in section 6c, ahead.

642 *e. SIC-SST-SLP reemergence families*

643 We have identified families of coupled NLSA SIC modes which are able to reproduce the
644 reemergence signal of the raw SIC data. Next, we focus on the spatiotemporal evolution
645 of these families, and their associated SST and SLP patterns. As noted earlier, there are
646 strong correlations between the temporal modes of SIC, SST, and SLP. We use this fact to
647 augment the families \mathcal{F}_1^M , \mathcal{F}_2^M , and \mathcal{F}_1^O with associated SST and SLP modes.

648 The low-frequency mode of \mathcal{F}_1^M is L_1^{SIC} . Performing correlations between this mode and
649 all low-frequency SST and SLP PCs, we find maximum correlations of -0.99 with L_1^{SST} and
650 -0.69 with L_3^{SLP} . Similarly, for the L_2^{SIC} mode of \mathcal{F}_2^M , we find maximum correlations of -0.93
651 with L_2^{SST} and 0.64 with L_1^{SLP} . For the observational family, \mathcal{F}_1^O , we find that L_1^{SIC} has
652 maximum correlations of 0.998 with L_1^{SST} and -0.81 with L_1^{SLP} . Note that the low-frequency
653 mode correlations are higher between SIC and SST than between SIC and SLP, indicating
654 that the temporal co-variability between SIC and SST is somewhat stronger.

655 Each family consists of a low-frequency mode and associated annual and semiannual
656 intermittent modes. In order to form the augmented families, we identify the intermittent

657 modes associated with the low-frequency SST and SLP modes identified above. Based on
 658 the envelope correlations shown in Fig. 6, we define the following augmented families:

$$\begin{aligned}\mathcal{F}_1^M &= \{L_1^{\text{SIC}}, I_{\{1,2,7,8\}}^{\text{SIC}}, L_1^{\text{SST}}, I_{\{2,3,8,9\}}^{\text{SST}}, L_3^{\text{SLP}}, I_{\{7,8\}}^{\text{SLP}}\}, \\ \mathcal{F}_2^M &= \{L_2^{\text{SIC}}, I_{\{3,4,9,10,11\}}^{\text{SIC}}, L_2^{\text{SST}}, I_{\{5,6,11\}}^{\text{SST}}, L_1^{\text{SLP}}, I_{\{1,2,9,10\}}^{\text{SLP}}\}, \\ \mathcal{F}_1^O &= \{L_1^{\text{SIC}}, I_{\{1,2,5,6\}}^{\text{SIC}}, L_1^{\text{SST}}, I_{\{1,2,7,8\}}^{\text{SST}}, L_1^{\text{SLP}}, I_{\{1\}}^{\text{SLP}}\}.\end{aligned}$$

659 Here, the intermittent mode indices are given in braces for each variable.

660 6. Sea-ice reemergence mechanisms

661 a. SST–sea-ice reemergence mechanism

662 We now examine the sea-ice reemergence mechanisms suggested by the SIC-SST-SLP
 663 families defined above. Bushuk et al. (2014) showed that low-dimensional families of NLSA
 664 modes produce an SST–sea-ice reemergence mechanism in the North Pacific sector which
 665 is consistent with that proposed by Blanchard-Wrigglesworth et al. (2011). Can a similar
 666 mechanism be observed in Arctic NLSA modes? In both the model and observations, the
 667 answer is yes.

668 Figure 13 shows spatial reconstructions of SIC, SST, and SLP using family \mathcal{F}_1^M . These
 669 spatial patterns are composites, produced by averaging over all times where $L_1^{\text{SIC}}(t) > 1$
 670 (which corresponds to 17% of the data). Similar patterns, with opposite sign, are obtained
 671 by compositing over times when $L_1^{\text{SIC}}(t)$ is in negative phase. This figure shows four months
 672 of the year, but the time evolution of \mathcal{F}_1^M , shown in Movie 5 of the supplementary material,
 673 is much more illuminating.

674 In the winter months of January–March, we observe strong negative sea-ice anomalies
 675 in the Barents Sea and strong positive anomalies in the Bering and Labrador Seas. These
 676 anomalies reach their maximum southerly extent in March. We observe SST anomalies of
 677 opposite sign, which are roughly spatially coincident with the sea-ice anomalies, but also

678 extend further south in each of the three seas. Note that in March the Kara sea, the
679 northern Bering Sea and the northern Labrador Sea are all SST anomaly-free. The ice
680 anomalies move northward and weaken over the melt season, which begins in April. In June,
681 the ice anomalies in the Barents-Kara region are located primarily in the Kara sea. Also,
682 the Bering and Labrador anomalies have moved into the northern parts of these seas and
683 weakened substantially.

684 As the ice anomalies move northward, they imprint an anomaly of opposite sign in the
685 SST field. In particular, the previously anomaly-free Kara and northern Bering and Labrador
686 Seas now have strong SST anomalies. The ice continues to retreat northwards over the melt
687 season, reaching its minimum extent in September. In September the sea-ice anomalies
688 are extremely weak in the Barents-Kara, Bering, and Labrador Seas, yet each of these seas
689 has retained an SST anomaly. The SST anomaly retained in the Barents-Kara and Bering
690 Seas is particularly strong, with a weaker anomaly in the Labrador Sea. As the growth
691 season begins, the ice moves southward, interacts with the SST anomalies that have been
692 stored over the summer months, and reinherits anomalies of the same sign as the previous
693 spring. In December, we observe that most of the summer imprinted SST anomalies have
694 disappeared, and the sea-ice anomalies have reemerged with the same sign as the spring
695 anomalies. This reemergence family is typically active for a 2-8 year period, during which
696 we observe reemerging sea-ice anomalies of a consistent sign (see Movie 5).

697 We observe a similar SST–sea-ice reemergence mechanism in family \mathcal{F}_2^M , shown in Fig. 14
698 and Movie 6 of the supplementary material. This figure is based on a composite over all
699 times in which $L_2^{\text{SIC}} > 1$ (which corresponds to 16% of the data). This family exhibits
700 strong winter sea-ice anomalies in the Bering and Labrador Seas, which are out of phase
701 with each other. These anomalies disappear over the melt season, leaving an SST imprint in
702 the northern parts of these seas in June and September. We observe a sea-ice reemergence
703 during the growth season, as the SST anomalies are converted into ice anomalies. This
704 family does not have a strong signal in the Barents-Kara Seas.

705 The observational family, \mathcal{F}_1^O , displays a clear sea-ice reemergence, which is active pri-
706 marily in the Barents-Kara, Bering, Okhotsk, Labrador, and Greenland Seas (Movie 7). This
707 family, shown for the year 1991 in Fig. 15, also displays the SST–sea-ice reemergence mech-
708 anism, but in a slightly less clean manner than the model output. \mathcal{F}_1^O has positive winter
709 sea-ice anomalies in the Bering and Labrador Seas, and negative anomalies in the Barents-
710 Kara, Greenland and Okhotsk Seas. The family has winter SST anomalies of opposite sign
711 to these sea-ice anomalies, which extend southward of the sea-ice anomalies. Comparing the
712 March panels to the June and September panels, an SST imprinting can be observed in the
713 Barents-Kara Sea and, to a lesser extent, the Labrador and Bering Seas. Sea-ice anomalies
714 of the same sign reappear in the fall, and this pattern roughly repeats the following year.

715 The reemergence families are able to capture the SST–sea-ice mechanism of Blanchard-
716 Wrigglesworth et al. (2011), previously only accessible via time correlation analysis of raw
717 sea-ice and SST fields. This mode-based representation of reemergence allows one to track
718 the temporal variability and strength of the SST–sea-ice reemergence mechanism, as will be
719 done ahead in section 6c. Also, the low-dimensionality of these families has implications for
720 predictability, since a small number of predictors (specifically, the low-frequency modes of
721 the families) define the amplitude and sign of reemergence events.

722 *b. Sea-ice teleconnections and reemergence via low-frequency SLP variability*

723 Movies 5-7 reveal consistent phase relationships between sea-ice anomalies in the Barents-
724 Kara, Bering, and Labrador Seas. The SST mechanism described above provides a local
725 mechanism for sea-ice reemergence, but does not explain this phase-locking between geo-
726 graphically disconnected seas. We find that the SLP patterns of \mathcal{F}_1^M , \mathcal{F}_2^M , and \mathcal{F}_1^O (shown
727 in the third column of Figs. 13, 14, and 15) provide pan-Arctic scale teleconnections between
728 these different regions.

729 We begin with family \mathcal{F}_1^M (Fig. 13), which has an SLP pattern closely resembling the
730 DA. This pattern is characterized by four main centers of action: pressure anomalies of

731 the same sign over Greenland and Northwest North America and opposite-signed anomalies
732 over Western Russia and Eastern Siberia. The geostrophic winds associated with this SLP
733 pattern are primarily meridional, blowing across the Arctic from the Bering to the Barents-
734 Kara Seas, or vice versa. We find that the ice advection and surface air temperature advection
735 associated with these large-scale winds is consistent with the observed phase relationships
736 in regional sea-ice anomalies.

737 From January–March, the dipole anomaly is very active, with strong northerly winds
738 over the Bering Sea and strong southerly winds over the Barents-Kara Seas. The northerly
739 winds advect cold Arctic air over the Bering Sea and also push the ice edge southwards
740 and advect additional ice into the sea. Each of these effects encourages the formation of
741 a positive sea-ice anomaly in the Bering Sea. Similarly, the Barents-Kara Seas experience
742 warm southerly winds, which melt additional ice, and also push the ice edge northward,
743 contributing to the observed negative sea-ice anomaly. Also, the SLP anomaly centered
744 over Greenland produces northerly geostrophic winds over the Labrador Sea, contributing
745 to its positive sea-ice anomalies for the same reasons. The SLP anomalies and corresponding
746 winds weaken substantially over the summer months, as do the sea-ice anomalies in each
747 of these regions. In October, the SLP anomalies begin to reappear with the same sign and
748 a similar spatial pattern to the previous winter. This coincides with the beginning of the
749 sea-ice growth season and the reemergence of ice anomalies from the previous spring. In
750 December, we observe a strong dipole SLP anomaly, and, again, observe sea-ice anomalies
751 in the Bering, Barents-Kara and Labrador Seas, which are physically consistent with this
752 pattern.

753 Besides explaining the observed teleconnection in sea-ice anomalies, these SLP patterns
754 also suggest an SLP–sea-ice reemergence mechanism via their winter-to-winter regime per-
755 sistence. L_3^{SLP} , the low-frequency SLP mode of \mathcal{F}_1^M , has a strong one-year autocorrelation of
756 0.70. Because SLP anomalies produce a significant sea-ice response, recurring SLP patterns
757 will produce recurring sea-ice patterns. Thus, the observed winter-to-winter persistence of

758 the SLP patterns of \mathcal{F}_1^M provides a candidate mechanism for sea-ice reemergence.

759 As mentioned earlier in section 4c, the SLP patterns of \mathcal{F}_1^M represent a low-pass filtered
760 version of the full atmospheric signal. The SLP patterns of \mathcal{F}_1^M should be thought of as a
761 slowly evolving atmospheric circulation regime, rather than a snapshot of the full SLP field
762 at each point in time. For example, the temporal evolution of the full SLP field is similar to
763 the time series of PC_1^{SLP} in Fig. 8, whereas the SLP patterns of \mathcal{F}_1^M are similar to the low-pass
764 filtered PC (red curve in Fig. 8). It is the persistence of the atmospheric circulation regime
765 of \mathcal{F}_1^M that provides a plausible mechanism for sea-ice reemergence. Sea-ice anomalies are
766 known to have a persistence of 2-5 months (Blanchard-Wrigglesworth et al. 2011), therefore
767 the sea-ice anomalies at a given time represent an integrated response to earlier atmospheric
768 and oceanic forcing. Given this, one would expect that sea-ice anomalies are not strongly
769 dependent on the chaotic month-to-month fluctuations of the atmosphere, but are more
770 dependent on a temporally smoothed version of this fluctuating field. Therefore, the low-
771 pass filtered SLP patterns of \mathcal{F}_1^M provide a plausible physical link between atmospheric
772 and sea-ice variability. The study of Blanchard-Wrigglesworth et al. (2011) dismisses SLP
773 persistence as a source of sea-ice reemergence because of the low one-month autocorrelation
774 of the SLP pattern that best explains changes in sea-ice extent. Here, we argue that the
775 low-frequency component of similar SLP patterns may play an important role in sea-ice
776 reemergence.

777 Similar relationships between sea-ice and SLP anomalies are also observed in family \mathcal{F}_2^M
778 (Fig. 14), which has an annular SLP pattern resembling the AO, and a one-year autocorre-
779 lation of 0.41. Similar to \mathcal{F}_1^M , these SLP patterns are strongly active over the winter months
780 (October–March), and fairly inactive over the summer months. The geostrophic winds of
781 this pattern are primarily zonal, but also have a meridional component, which affects sea
782 ice via surface air temperature advection. In January–March, there are northeasterly winds
783 over the Bering Sea, southeasterly winds over Labrador Sea, and northeasterly winds over
784 the Barents-Kara Seas, with corresponding positive, negative, and positive sea-ice anoma-

785 lies, respectively. The SLP anomalies become small over the summer months, and reappear
786 during the fall months with the same sign as the previous winter. With the reappearance
787 of these SLP anomalies, we observe an ice reemergence, which is particularly strong in the
788 Bering and Labrador Seas.

789 The relationship between SLP and sea ice is somewhat less clear in the observations than
790 in the model. Column three of Fig. 15 shows the \mathcal{F}_1^O SLP patterns for 1991, a year when the
791 family was active. In January–March, there is an AO-like SLP pattern producing northerly
792 winds over the Labrador Sea and southerly winds over the Barents-Kara Seas. We observe
793 corresponding positive and negative sea-ice anomalies in these seas, analogous to what was
794 observed in \mathcal{F}_2^M . However, the SLP patterns differ in the North Pacific. There is mini-
795 mal advection over the Bering Sea, as a high-pressure anomaly is centered directly over it.
796 This anomaly produces southerly winds over the Sea of Okhotsk, which are consistent with
797 the negative sea-ice anomaly. On the other hand, the SLP patterns do not provide a clear
798 explanation, in terms of meridional wind, for the positive Bering sea-ice anomalies. Com-
799 pared to \mathcal{F}_2^M , these SLP patterns do not decorrelate as strongly over the summer months,
800 and a negative SLP anomaly is retained over the pole, which also shifts onto the Eurasian
801 continent over the summer months. The anomaly strengthens during the fall, producing
802 similar winds and sea-ice patterns to the previous winter. One notable difference between
803 the observational and model SLP families is the spatial stationarity of the SLP patterns.
804 The SLP patterns of \mathcal{F}_1^M and \mathcal{F}_2^M are relatively fixed in space and pulse on and off with the
805 annual cycle. The \mathcal{F}_1^O SLP patterns also pulse with the annual cycle, yet are transient in
806 space. The SLP centers-of-action advect substantially over the course of a year.

807 Given the seemingly similar sea-ice anomalies of \mathcal{F}_1^M and \mathcal{F}_1^O , a natural question is why
808 these families have such different atmospheric patterns. A closer analysis of the sea-ice
809 variability of each family reveals clear differences between the two. For each family, we
810 compute the proportion of sea-ice variance in a given region, relative to the variance of the
811 full Arctic domain. We find that \mathcal{F}_1^M contains 24% of its variance in the Bering Sea, 22%

812 in the Barents-Kara Seas, and 8% in the Labrador Sea. Conversely, \mathcal{F}_1^O contains 5% of
813 its variance in the Bering Sea, 35% in the Barents-Kara Seas, and 14% in the Labrador
814 Sea. Therefore, the dominant sea-ice feature of \mathcal{F}_1^M is the dipole between the Bering and
815 Barents-Kara Seas, whereas the dominant feature of \mathcal{F}_1^O is the dipole between the Labrador
816 and Barents-Kara Seas. The corresponding atmospheric circulation patterns of each family
817 act to reinforce these dominant sea-ice anomalies, and have significantly different spatial
818 patterns.

819 It should be noted that the data analysis approach employed here is capable of identifying
820 correlation, but not causality. In particular, we have not quantified the relative importance
821 of the ocean and the atmosphere in producing sea-ice reemergence. Also, we have identified
822 SLP modes with interannual to decadal variability, but have not provided a mechanism for
823 this observed variability. We speculate that, rather than intrinsic atmospheric variability,
824 this low-frequency variability of the atmosphere results from SST or sea-ice forcing. The
825 generation of low-frequency atmospheric variability has been widely studied, with many
826 authors suggesting that extratropical and tropical SST anomalies are capable of driving
827 low-frequency variability in the atmosphere (Lau and Nath 1990; Latif and Barnett 1994;
828 Trenberth and Hurrell 1994; Weng and Neelin 1998; Selten et al. 1999; Robertson et al. 2000;
829 Kushnir et al. 2002; Czaja and Frankignoul 2002). Other authors (e.g., Mysak and Venegas
830 1998), have suggested that sea-ice anomalies could drive low-frequency atmospheric patterns,
831 but modeling studies have suggested that the atmospheric response is quite weak compared
832 with the typical magnitude of atmospheric anomalies (Alexander et al. 2004; Magnusdottir
833 et al. 2004). Therefore, we speculate that anomalous SST forcing is the most likely candidate
834 for the observed low-frequency SLP patterns, but more study is required on this problem.
835 These unanswered questions could be investigated in a future study involving a hierarchy of
836 GCM experiments.

838 We now establish a set of reemergence metrics for sea ice, SST, and SLP, by which one
 839 can judge the activity of sea-ice reemergence and associated mechanisms in different regions.
 840 These metrics, computed for the reconstructed fields of each family, quantify the intensity
 841 and sign of ice reemergence events. We focus on the values of these metrics in the Bering,
 842 Barents-Kara, and Labrador Seas. The sea-ice metric is defined as the integrated (area-
 843 weighted) SIC anomaly in a given region. We define the SLP metric as the maximum value
 844 of the meridional geostrophic wind over a given region. This is a proxy for the amount of
 845 warm/cold air advection and northward/southward ice advection over a given region. The
 846 SST metric is defined as the integrated (area-weighted) SST anomalies in the portion of the
 847 seas that are imprinted by summer SST anomalies. Specifically, we compute the integrated
 848 SST anomalies in the Kara sea (75°E – 100°E and 65°N – 80°N), the northern Bering Sea
 849 (165°E – 160°W and 60°N – 65°N), and the northern Labrador Sea (70°W – 40°W and 60°N
 850 – 80°N). It is helpful to compare the metrics, plotted in Figs. 16–18, to Movies 5–7 which
 851 show the dynamical evolution of the corresponding fields for the same time period.

852 Figure 16 shows \mathcal{F}_1^M metrics for 100 years of model output. We observe a number
 853 of reemergence events, characterized by periods in which the sea-ice metric is large, with
 854 consistent sign, over a number of successive winters. For example, notable periods of active
 855 reemergence occur during years 101–106, 128–131, 146–155, and 175–179. The sea-ice phase
 856 relationships for this family are striking, with strong positive correlation (0.95) between the
 857 Bering and the Labrador Seas and strong anti-correlation (-0.95) between the Bering and
 858 Barents-Kara Seas. The SST metric reveals the SST-sea-ice reemergence mechanism, as years
 859 with large ice metrics have large SST metrics of the opposite sign (note the anti-correlation
 860 of like-colored curves in panels A and B). During reemergence events, the SST metrics are
 861 close to zero in the winter months and grow large in the summer months as the sea-ice
 862 anomalies imprint the SST field. These SST metrics also show a clear in-phase relationship
 863 between the Bering and Labrador Seas and out-of-phase relationship between the Bering and

864 Barents-Kara Seas. The SLP metric is clearly out-of-phase with the sea-ice metric, which
865 illustrates the sea ice-SLP reemergence mechanism, since positive (negative) meridional wind
866 anomalies produce negative (positive) sea-ice anomalies. During reemergence events, in the
867 Bering and Labrador Seas, we observe that the SLP metric is large over the winter and close
868 to zero over the summer. In the Barents-Kara Sea, we observe more persistence, as the
869 family maintains its wind anomalies throughout an entire reemergence event.

870 Figure 17 shows the metrics for family \mathcal{F}_2^M . Again, we observe very strong phase relation-
871 ships in sea-ice anomalies, with in-phase anomalies between the Barents-Kara and Bering
872 Seas and out-of-phase anomalies between the Bering and Labrador Seas. The SST metric
873 displays strong SST–sea-ice reemergence mechanisms in the Labrador and Bering Seas. Also,
874 as noted in section 5c, there is not a clear SST–sea-ice mechanism in the Barents-Kara Sea.
875 The SLP metric has a strong signal in the Labrador Sea, which is large in winter and small
876 in summer, and out-of-phase with the sea-ice anomalies. The SLP–sea-ice mechanism is less
877 strong in the Barents-Kara and Bering Seas, yet we do observe persistent wind anomalies
878 which are out-of-phase with the sea-ice anomalies.

879 We show metrics for \mathcal{F}_1^O in Fig. 18. This family exhibits a strong SST–sea-ice reemergence
880 mechanism in the Barents-Kara Sea. The SST signal is very weak in the Bering Sea, and
881 in the Labrador Sea it tends to persist over periods of reemergence, rather than being
882 imprinted each summer. The wind anomalies in the Labrador and Barents-Kara Seas are
883 consistent with the sea ice-SLP reemergence mechanism. As noted earlier, the Bering Sea
884 wind anomalies are not consistent with the sea-ice anomalies. Rather, we observe that the
885 wind anomalies are inconsistent (in-phase) with the sea-ice anomalies.

886 *d. Regional sea-ice relationships conditional on SLP modes*

887 The reemergence families suggest a number of sea-ice teleconnections which are related
888 to large-scale SLP patterns. Are these regional teleconnections visible in the raw SIC data?
889 Are the teleconnections strengthened by conditioning on certain low-frequency SLP modes

890 being active? To answer these questions, we select pairs of regions and compute lagged cross-
 891 correlations in total sea-ice area anomalies of the raw data between these regions. Note that
 892 the cross-correlations are obtained by computing a time series of sea-ice area anomalies for
 893 each region, and performing lagged correlations between these two time series. Our choice
 894 of regions and SLP modes is guided by the reemergence families. We consider the regions
 895 and SLP pattern that display the strongest teleconnection for each family.

896 The results are shown in Fig. 19, for months of the year with sea-ice coverage in the
 897 marginal ice zones (December–May) and for lags of -23 to 23 months. Panels A and B show
 898 lagged cross-correlations between the Barents-Kara and Bering Seas for the raw CCSM3
 899 data and conditional on $|L_3^{\text{SLP}}| > 1.5$ (corresponds to 14% of the data), respectively. This
 900 corresponds to the primary teleconnection of \mathcal{F}_1^M . All correlations plotted in color are
 901 significant at the 95% level, based on a t -distribution statistic. In the raw data, we observe
 902 negative correlations between the Bering and Barents-Kara Seas, which are strongest at lags
 903 of -6 to 6 months. There is a dramatic strengthening of these negative correlations when
 904 conditioned on an active L_3^{SLP} mode (the DA mode). We also observe that the correlations
 905 are more persistent when the DA mode is active. Another interesting feature is the clear
 906 bias in correlations towards lags in which Bering anomalies lead Barents-Kara anomalies.
 907 The analogous correlations, corresponding to family \mathcal{F}_2^M , are shown in panels C and D for
 908 the Labrador and Bering Seas and for SLP mode L_1^{SLP} (the AO mode). These correlations
 909 are very small compared with panels A and B. The raw data displays very little correlation
 910 structure and weak correlations, that are primarily negative, emerge after conditioning on
 911 the AO mode. It should be noted that the limb of negative correlations, with Bering lagging
 912 Labrador, corresponds to summer sea-ice anomalies in the Bering Sea, which are extremely
 913 weak. Therefore, this limb has questionable significance.

914 Panels E and F show cross-correlations between the Barents-Kara and Labrador Seas for
 915 the HadISST dataset, conditional on $|L_1^{\text{SLP}}| > 1$ (corresponds to 35% of the data). Note
 916 that we use a value of 1 rather than 1.5 for the conditional correlations because of the

917 shortness of the observational time series. Also, the shortness of the time series implies a
918 higher 95% significance level for correlations. We plot correlations using the same colorbar
919 as CCSM3 and simply white-out all correlations which are not significant at the 95% level.
920 The raw data displays some negative correlation, but a dramatic strengthening is observed
921 when conditioning on an active AO mode. The limb of white in panel F, extending from
922 (May, +3) to (Dec, +9) corresponds to lagged correlations with summer months. At lags
923 beyond this limb, we observe strong negative correlations. This feature is a reemergence of
924 anti-correlation between the Barents-Kara and Labrador Seas. The reemergence structure is
925 less clear for negative lags, where the Labrador leads the Barents-Kara, however we generally
926 observe anti-correlation between the two seas, which is significantly stronger than the raw
927 data.

928 **7. Conclusions**

929 We have studied Arctic sea-ice reemergence (Blanchard-Wrigglesworth et al. 2011) in a
930 comprehensive climate model and observations. This study has documented the regional
931 and temporal details of sea-ice reemergence and illustrated two potential reemergence mech-
932 anisms, involving SST and SLP persistence, respectively. We have used coupled NLSA (Gi-
933 annakis and Majda 2012b, 2013; Bushuk et al. 2014), a nonlinear data analysis technique for
934 multivariate timeseries, to analyze the co-variability of Arctic SIC, SST, and SLP. Coupled
935 NLSA was applied to a 900-year equilibrated control integration of CCSM3, yielding spa-
936 tiotemporal modes, analogous to EEOFs, and temporal patterns, analogous to PCs. Modes
937 were also extracted from 34 years of observational data, using SIC and SST observations from
938 HadISST and SLP reanalysis from ERA-Interim. In both the model and observations, these
939 NLSA modes capture three distinct types of temporal behavior: periodic, low-frequency,
940 and intermittent variability. The low-frequency modes have spatial patterns that closely
941 resemble the leading EOFs of each variable. In particular, the low-frequency SLP modes

942 correlate strongly with the well-known Arctic Oscillation (AO, Thompson and Wallace 1998)
943 and Arctic Dipole Anomaly (DA, Wu et al. 2006) patterns of SLP variability. The temporal
944 patterns of the low-frequency SLP modes, obtained here without any preprocessing of the
945 raw data, closely resemble a low-pass filtered version of the corresponding PCs obtained via
946 EOF analysis.

947 Performing time-lagged pattern correlations, we have found clear pan-Arctic sea-ice
948 reemergence signals in the model and observations. The lagged pattern correlation approach
949 employed in this study reveals a stronger reemergence signal in observations than previous
950 studies on reemergence (Blanchard-Wrigglesworth et al. 2011; Day et al. 2014). Using cou-
951 pled NLSA modes, we have found low-dimensional families that are able to reproduce the
952 reemergence signal of the raw SIC data. Intriguingly, these families explain a relatively small
953 portion of the raw SIC variance, yet when removed from the raw data the resulting signal
954 exhibits significantly weaker reemergence. Moreover, the associated SST and SLP patterns
955 of these families demonstrate two possible reemergence mechanisms, consistent with those
956 proposed by Blanchard-Wrigglesworth et al. (2011) and Deser et al. (2002). The SST–sea-ice
957 reemergence mechanism, in which spring sea-ice anomalies are imprinted and stored as sum-
958 mer SST anomalies, is clearly active in the Barents-Kara, Bering, and Labrador Seas. The
959 SLP–sea-ice mechanism, in which sea-ice anomalies reemerge due to the winter-to-winter
960 persistence of low-pass filtered SLP anomalies (atmospheric regimes), is also observed in
961 these regions, with the exception of the Bering Sea in the observational record.

962 A key finding of this study is that these reemergence patterns are part of a pan-Arctic
963 scale organization involving SLP teleconnection patterns. In particular, we have found strong
964 phase relationships between sea-ice reemergence events in geographically distinct regions.
965 Unable to explain this teleconnection in terms of purely local SST anomalies, we find clear
966 relationships between regional sea-ice anomalies and large-scale SLP variability. In CCSM3,
967 an out-of-phase relationship between the Bering/Labrador and Barents-Kara Seas is found
968 to be consistent with the phase and amplitude of the DA mode. Similarly, an out-of-phase

969 relationship between the Bering/Barents-Kara and Labrador Seas is found to be consistent
970 with the phase and amplitude of the AO mode. In observations, the AO mode is able
971 to explain the strong out-of-phase anomalies of the Barents-Kara and Labrador Seas, but
972 cannot explain the weaker anomalies of the Bering Sea. These regional phase relationships
973 are weakly visible in the raw SIC data, and are significantly strengthened by conditioning
974 on an appropriate SLP mode (the AO or DA) being active.

975 Another key aspect of this study is the regional and temporal characterization of sea-
976 ice reemergence. We have identified significant regional differences in reemergence between
977 the model and observations, particularly in the Labrador Sea and the North Pacific sec-
978 tor, despite their pan-Arctic agreement. We have also found that reemergence events and
979 mechanisms have significant temporal variability, and that the low-frequency modes of the
980 reemergence families act as effective predictors of periods of active or quiescent reemergence.
981 A set of reemergence metrics has been created, by which one can judge the strength and
982 sign of sea-ice reemergence events, and the associated SST and SLP mechanisms.

983 In this study, we have demonstrated two plausible mechanisms for sea-ice reemergence,
984 involving the atmosphere and the ocean, but which mechanism is most crucial in producing
985 ice reemergence? Is sea-ice reemergence a fully coupled phenomenon, or does it also occur
986 in more idealized situations? This data analysis study has identified correlation, but not
987 causation. An interesting subject for future work would be to perform a suite of coupled
988 model experiments to study this question of causality.

989 *Acknowledgments.*

990 We thank Ed Blanchard-Wrigglesworth and two anonymous reviewers for valuable com-
991 ments that helped improve the manuscript. D. Giannakis and A.J. Majda wish to acknowl-
992 edge support from ONR MURI grant 25-74200-F7112. The research of D. Giannakis is
993 partially supported by ONR DRI grant N00014-14-1-0150. M. Bushuk is supported as a
994 graduate student under this grant. M. Bushuk also received support from the Center for

995 Prototype Climate Modeling at NYU Abu Dhabi Research Institute, and NSERC PGS-D
996 award 404213.

REFERENCES

- 999 Alexander, M. A., U. S. Bhatt, J. E. Walsh, M. S. Timlin, J. S. Miller, and J. D. Scott,
1000 2004: The atmospheric response to realistic Arctic sea ice anomalies in an AGCM during
1001 winter. *J. Climate*, **17** (5), 890–905.
- 1002 Alexander, M. A., C. Deser, and M. S. Timlin, 1999: The reemergence of SST anomalies in
1003 the North Pacific Ocean. *J. Climate*, **12**, 2419–2433.
- 1004 Aubry, N., W.-Y. Lian, and E. S. Titi, 1993: Preserving symmetries in the proper orthogonal
1005 decomposition. *SIAM J. Sci. Comput.*, **14**, 483–505.
- 1006 Berry, T., R. Cressman, Z. Greguric-Ferencek, and T. Sauer, 2013: Time-scale separation
1007 from diffusion-mapped delay coordinates. *SIAM J. Appl. Dyn. Sys.*, **12**, 618–649.
- 1008 Blanchard-Wrigglesworth, E., K. C. Armour, C. M. Bitz, and E. DeWeaver, 2011: Persistence
1009 and inherent predictability of Arctic sea ice in a GCM ensemble and observations. *J.*
1010 *Climate*, **24**, 231–250.
- 1011 Broomhead, D. S. and G. P. King, 1986: Extracting qualitative dynamics from experimental
1012 data. *Phys. D*, **20** (2–3), 217–236, doi:10.1016/0167-2789(86)90031-x.
- 1013 Bushuk, M., D. Giannakis, and A. J. Majda, 2014: Reemergence mechanisms for North
1014 Pacific sea ice revealed through nonlinear Laplacian spectral analysis. *J. Climate*, **27**,
1015 6265–6287.
- 1016 Cavalieri, D. J. and C. L. Parkinson, 2012: Arctic sea ice variability and trends, 1979-2010.
1017 *The Cryosphere*, **6** (4), 881–889, doi:10.5194/tc-6-881-2012.
- 1018 Collins, W. D., et al., 2004: Description of the NCAR Community Atmosphere Model (CAM
1019 3.0). Tech. Rep. TN-464+STR, National Center for Atmospheric Research, 226 pp.

- 1020 Collins, W. D., et al., 2006: The Community Climate System Model version 3 (CCSM3). *J.*
1021 *Climate*, **19**, 2122–2143.
- 1022 Czaja, A. and C. Frankignoul, 2002: Observed impact of Atlantic SST anomalies on the
1023 North Atlantic Oscillation. *J. Climate*, **15** (6), 606–623.
- 1024 Day, J., S. Tietsche, and E. Hawkins, 2014: Pan-Arctic and regional sea ice predictability:
1025 Initialization month dependence. *J. Climate*, **27** (12), 4371–4390.
- 1026 de Cotlogon, G. and C. Frankignoul, 2003: On the persistence of winter sea surface temper-
1027 ature in the North Atlantic. *J. Climate*, **16**, 1364–1377.
- 1028 Dee, D. P., et al., 2011: The ERA-Interim reanalysis: configuration and performance of the
1029 data assimilation system. *Q.J.R. Meteorol. Soc.*, **137**, 553–597, doi:10.1002/qj.828.
- 1030 Deser, C., M. Holland, G. Reverdin, and M. S. Timlin, 2002: Decadal variations in Labrador
1031 sea ice cover and North Atlantic sea surface temperatures. *J. of Geophys. Res.*, **107**, C5,
1032 doi:10.1029/2000JC000683.
- 1033 Deser, C., J. E. Walsh, and M. S. Timlin, 2000: Arctic sea ice variability in the context of
1034 recent atmospheric circulation trends. *J. Climate*, **13**, 617–633.
- 1035 Francis, J. A. and E. Hunter, 2007: Drivers of declining sea ice in the Arctic winter: A tale
1036 of two seas. *Geophys. Res. Lett.*, **34** (17), doi:10.1029/2007GL030995.
- 1037 Ghil, M., et al., 2002: Advanced spectral methods for climatic time series. *Rev. Geophys.*,
1038 **40**(1), 3.1–3.41.
- 1039 Giannakis, D. and A. J. Majda, 2012a: Comparing low-frequency and intermittent variability
1040 in comprehensive climate models through nonlinear Laplacian spectral analysis. *Geophys.*
1041 *Res. Lett.*, **39**, L10 710, doi:10.1029/2012GL051575.
- 1042 Giannakis, D. and A. J. Majda, 2012b: Nonlinear Laplacian spectral analysis for time series
1043 with intermittency and low-frequency variability. *Proc. Natl. Acad. Sci.*, **109**, 2222–2227.

- 1044 Giannakis, D. and A. J. Majda, 2013: Nonlinear Laplacian spectral analysis: Capturing
1045 intermittent and low-frequency spatiotemporal patterns in high-dimensional data. *Stat.*
1046 *Anal. Data Min.*, **6 (3)**, 180–194, doi:10.1002/sam.11171.
- 1047 Giannakis, D. and A. J. Majda, 2014: Data-driven methods for dynamical systems: Quanti-
1048 fying predictability and extracting spatiotemporal patterns. *Mathematical and Computa-*
1049 *tional Modeling: With Applications in Engineering and the Natural and Social Sciences*,
1050 R. Melnik, Ed., Wiley, Hoboken, 288.
- 1051 Holland, M. M., C. Bitz, E. Hunke, W. Lipscomb, and J. Schramm, 2006: Influence of the
1052 sea ice thickness distribution on polar climate in CCSM3. *J. Stat. Phys.*, **19**, 2398–2414.
- 1053 Johnson, M. A., A. Y. Proshutinsky, and I. V. Polyakov, 1999: Atmospheric patterns forcing
1054 two regimes of Arctic circulation: A return to anticyclonic conditions? *Geophys. Res. Lett.*,
1055 **26 (11)**, 1621–1624.
- 1056 Kay, J. E., M. M. Holland, and A. Jahn, 2011: Inter-annual to multi-decadal Arctic sea
1057 ice extent trends in a warming world. *Geophys. Res. Lett.*, **38**, L15708, doi:10.1029/
1058 2011GL048008.
- 1059 Kushnir, Y., W. Robinson, I. Bladé, N. Hall, S. Peng, and R. Sutton, 2002: Atmospheric
1060 GCM response to extratropical SST anomalies: Synthesis and evaluation*. *J. Climate*,
1061 **15 (16)**, 2233–2256.
- 1062 Latif, M. and T. P. Barnett, 1994: Causes of decadal climate variability over the North
1063 Pacific and North America. *Science*, **266 (5185)**, 634–637.
- 1064 Lau, N.-C. and M. J. Nath, 1990: A general circulation model study of the atmospheric
1065 response to extratropical SST anomalies observed in 1950-79. *J. Climate*, **3 (9)**, 965–989.
- 1066 L’Heureux, M. L., A. Kumar, G. D. Bell, M. S. Halpert, and R. W. Higgins, 2008: Role of

1067 the Pacific-North American (PNA) pattern in the 2007 Arctic sea ice decline. *Geophys.*
1068 *Res. Lett.*, **35** (**20**), doi:10.1029/2008GL035205.

1069 Magnusdottir, G., C. Deser, and R. Saravanan, 2004: The effects of North Atlantic SST
1070 and sea ice anomalies on the winter circulation in CCM3. Part I: Main features and storm
1071 track characteristics of the response. *J. Climate*, **17** (**5**), 857–876.

1072 Maslanik, J., S. Drobot, C. Fowler, W. Emery, and R. Barry, 2007: On the Arctic climate
1073 paradox and the continuing role of atmospheric circulation in affecting sea ice conditions.
1074 *Geophys. Res. Lett.*, **34** (**3**), doi:10.1029/2006GL028269.

1075 Moritz, R. E., C. M. Bitz, and E. J. Steig, 2002: Dynamics of recent climate change in the
1076 Arctic. *Science*, **297** (**5586**), 1497–1502.

1077 Mysak, L. A. and S. A. Venegas, 1998: Decadal climate oscillations in the Arctic: A new
1078 feedback loop for atmosphere-ice-ocean interactions. *Geophys. Res. Lett.*, **25** (**19**), 3607–
1079 3610.

1080 Overland, J. E. and M. Wang, 2005: The third Arctic climate pattern: 1930s and early
1081 2000s. *Geophys. Res. Lett.*, **32** (**23**), doi:10.1029/2005GL024254.

1082 Overland, J. E. and M. Wang, 2010: Large-scale atmospheric circulation changes are associ-
1083 ated with the recent loss of Arctic sea ice. *Tellus A*, **62** (**1**), 1–9, doi:10.1111/j.1600-0870.
1084 2009.00421.x.

1085 Polyakov, I. V. and M. A. Johnson, 2000: Arctic decadal and interdecadal variability. *Geo-*
1086 *phys. Res. Lett.*, **27** (**24**), 4097–4100.

1087 Proshutinsky, A. Y. and M. A. Johnson, 1997: Two circulation regimes of the wind-driven
1088 Arctic Ocean. *Journal of Geophysical Research: Oceans*, **102** (**C6**), 12 493–12 514, doi:
1089 10.1029/97JC00738.

1090 Rayner, N. A., D. E. Parker, E. B. Horton, C. K. Folland, L. V. Alexander, D. P. Rowell,
1091 E. C. Kent, and A. Kaplan, 2003: Global analyses of sea surface temperature, sea ice, and
1092 night marine air temperature since the late nineteenth century. *J. Geophys. Res.*, **108**,
1093 4407, doi:10.1029/2002JD002670.

1094 Rigor, I. G. and J. M. Wallace, 2004: Variations in the age of Arctic sea-ice and summer
1095 sea-ice extent. *Geophys. Res. Lett.*, **31 (9)**, doi:10.1029/2004GL019492.

1096 Rigor, I. G., J. M. Wallace, and R. L. Colony, 2002: Response of sea ice to the Arctic
1097 Oscillation. *J. Climate*, **15**, 2648–2663, doi:10.1175/1520-0442.

1098 Robertson, A. W., C. R. Mechoso, and Y.-J. Kim, 2000: The Influence of Atlantic Sea
1099 Surface Temperature Anomalies on the North Atlantic Oscillation*. *J. Climate*, **13 (1)**,
1100 122–138.

1101 Screen, J. A., I. Simmonds, and K. Keay, 2011: Dramatic interannual changes of perennial
1102 Arctic sea ice linked to abnormal summer storm activity. *Journal of Geophysical Research:*
1103 *Atmospheres*, **116 (D15)**, doi:10.1029/2011JD015847.

1104 Selten, F. M., R. Haarsma, and J. Opsteegh, 1999: On the mechanism of North Atlantic
1105 decadal variability. *J. Climate*, **12 (7)**, 1956–1973.

1106 Serreze, M. C., M. M. Holland, and J. Stroeve, 2007: Perspectives on the Arctic’s shrinking
1107 sea-ice cover. *Science*, **315 (5818)**, 1533–1536, doi:10.1126/science.1139426.

1108 Serreze, M. C., et al., 2003: A record minimum arctic sea ice extent and area in 2002.
1109 *Geophys. Res. Lett.*, **30 (3)**, doi:10.1029/2002GL016406.

1110 Smith, R. and P. Gent, 2004: Reference manual for the Parallel Ocean Program (POP):
1111 Ocean component of the Community Climate System Model (CCSM2.0 and 3.0). Tech.
1112 Rep. LAUR-02-2484, Los Alamos National Laboratory, 75 pp.

- 1113 Stroeve, J., M. M. Holland, W. Meier, T. Scambos, and M. Serreze, 2007: Arctic sea ice
1114 decline: Faster than forecast. *Geophys. Res. Lett.*, **34 (9)**, doi:10.1029/2007GL029703.
- 1115 Stroeve, J. C., V. Kattsov, A. Barrett, M. Serreze, T. Pavlova, M. Holland, and W. N. Meier,
1116 2012: Trends in Arctic sea ice extent from CMIP5, CMIP3 and observations. *Geophys.*
1117 *Res. Lett.*, **39 (16)**, doi:10.1029/2012GL052676.
- 1118 Thompson, D. W. J. and J. M. Wallace, 1998: The Arctic oscillation signature in the
1119 wintertime geopotential height and temperature fields. *Geophys. Res. Lett.*, **25**, 1297–1300,
1120 doi:10.1029/98GL00950.
- 1121 Timlin, M. S., M. A. Alexander, and C. Deser, 2002: On the reemergence of North Atlantic
1122 SST anomalies. *J. Climate*, **15**, 2707–2712.
- 1123 Trenberth, K. E. and J. W. Hurrell, 1994: Decadal atmosphere-ocean variations in the
1124 Pacific. *Climate Dynamics*, **9 (6)**, 303–319.
- 1125 Tsukernik, M., C. Deser, M. Alexander, and R. Tomas, 2010: Atmospheric forcing of Fram
1126 Strait sea ice export: A closer look. *Climate Dynamics*, **35 (7-8)**, 1349–1360, doi:10.1007/
1127 s00382-009-0647-z.
- 1128 Vautard, R. and M. Ghil, 1989: Singular Spectrum Analysis in nonlinear dynamics, with
1129 applications to paleoclimatic time series. *Phys. D*, **35**, 395–424, doi:10.1016/0167-2789(89)
1130 90077-8.
- 1131 von Storch, H. and F. W. Zwiers, 1999: *Statistical Analysis in Climate Research*. Cambridge
1132 University Press, 484 pp., doi:10.1017/CBO9780511612336.
- 1133 Walsh, J. E., W. L. Chapman, and T. L. Shy, 1996: Recent decrease of sea level pressure in
1134 the central Arctic. *J. Climate*, **9 (2)**, 480–486.
- 1135 Wang, J., J. Zhang, E. Watanabe, M. Ikeda, K. Mizobata, J. E. Walsh, X. Bai, and B. Wu,

- 1136 2009: Is the Dipole Anomaly a major driver to record lows in Arctic summer sea ice
1137 extent? *Geophys. Res. Lett.*, **36 (5)**, doi:10.1029/2008GL036706.
- 1138 Watanabe, E., J. Wang, A. Sumi, and H. Hasumi, 2006: Arctic Dipole Anomaly and its
1139 contribution to sea ice export from the Arctic Ocean in the 20th century. *Geophys. Res.
1140 Lett.*, **33 (23)**, doi:10.1029/2006GL028112.
- 1141 Weng, W. and J. D. Neelin, 1998: On the role of ocean-atmosphere interaction in midlatitude
1142 interdecadal variability. *Geophys. Res. Lett.*, **25 (2)**, 167–170.
- 1143 Wettstein, J. J. and C. Deser, 2014: Internal variability in projections of twenty-first-century
1144 Arctic sea ice loss: Role of the large-scale atmospheric circulation. *J. Climate*, **27**, 527–550,
1145 doi:10.1175/JCLI-D-12-00839.1.
- 1146 Wu, B., J. Wang, and J. E. Walsh, 2006: Dipole Anomaly in the winter Arctic atmosphere
1147 and its association with sea ice motion. *J. Climate*, **19**, 210–225, doi:10.1175/JCLI3619.1.
- 1148 Yi, D., L. A. Mysak, and S. A. Venegas, 1999: Decadal-to-interdecadal fluctuations of Arc-
1149 tic sea-ice cover and the atmospheric circulation during 1954–1994. *Atmosphere-Ocean*,
1150 **37 (4)**, 389–415.
- 1151 Zhang, J., M. Steele, D. A. Rothrock, and R. W. Lindsay, 2004: Increasing exchanges at
1152 Greenland-Scotland Ridge and their links with the North Atlantic Oscillation and Arctic
1153 sea ice. *Geophys. Res. Lett.*, **31 (9)**.

1154 List of Figures

- 1155 1 The regions of interest in this study: the Barents-Kara Seas (BK), the Labrador
 1156 Sea (LS), the Greenland Sea (GS), the Bering Sea (BER), and the Sea of
 1157 Okhotsk (OK). The Arctic domain is defined as all grid points north of 45°N. 52
- 1158 2 Schematic summarizing the flow of data in the coupled NLSA algorithm. 53
- 1159 3 Snapshots of the time series, power spectral density, and autocorrelation func-
 1160 tions for the CCSM3 SIC PCs (v_k) from coupled NLSA. Shown here for 50-year
 1161 portions of the 900-yr time series are the annual periodic (P_1^{SIC}) and semi-
 1162 annual periodic (P_3^{SIC}) modes, low-frequency modes (L_1^{SIC} and L_2^{SIC}), annual
 1163 intermittent modes (I_1^{SIC} and I_3^{SIC}), and semiannual intermittent modes (I_7^{SIC}
 1164 and I_9^{SIC}). The autocorrelation vertical scale is [-1,1]. The power spectral den-
 1165 sities (f_k) were estimated via the multitaper method with time-bandwidth
 1166 product $p = 6$ and $K = 2p - 1 = 11$ Slepian tapers. The effective half-
 1167 bandwidth resolution for the s monthly samples is $\Delta\nu = p/(s\delta t) = 1/150$
 1168 y^{-1} , where $\delta t = 1/12$ y is the sampling interval. 54
- 1169 4 Snapshots of the time series, power spectral density, and autocorrelation func-
 1170 tions for the CCSM3 SST PCs from coupled NLSA. Shown here are the annual
 1171 periodic (P_1^{SST}) and semiannual periodic (P_3^{SST}) modes, low-frequency modes
 1172 (L_1^{SST} , L_2^{SST} , and L_3^{SST}), annual intermittent modes (I_1^{SST} and I_3^{SST}), and semi-
 1173 annual intermittent modes (I_7^{SST}). The autocorrelation vertical scale is [-1,1]. 55
- 1174 5 Snapshots of the time series, power spectral density, and autocorrelation func-
 1175 tions for the CCSM3 SLP PCs from coupled NLSA. Shown here are the annual
 1176 periodic (P_1^{SLP}) and semiannual periodic (P_3^{SLP}) modes, low-frequency modes
 1177 (L_1^{SLP} , L_2^{SLP} , L_3^{SLP}), and intermittent modes (I_1^{SLP} , I_3^{SLP} , I_7^{SLP}). The autocor-
 1178 relation vertical scale is [-1,1]. 56

1179	6	Correlations between low-frequency modes and envelope functions for inter-	
1180		mittent modes. Mode pairs with large positive correlations indicate that the	
1181		low-frequency mode provides the modulating envelope for the intermittent	
1182		mode.	57
1183	7	Spatial patterns of selected sea ice, SST, and SLP NLSA modes. For each	
1184		mode, we plot the spatial pattern with largest variance (of the q spatial pat-	
1185		terns that make up the spatiotemporal pattern). Rows 1-3 show CCSM3	
1186		modes and row 4 shows observational modes, indicated by an O subscript.	
1187		The fields have been normalized to have a maximum absolute value of 1.	58
1188	8	Snapshots of the time series, power spectral density, and autocorrelation	
1189		functions for L_1^{SLP} , the leading low-frequency NLSA mode from CCSM3,	
1190		PC_1^{SLP} , the principal component corresponding to the leading EOF of SLP,	
1191		and $\langle \text{PC}_1^{\text{SLP}} \rangle$, a low-pass filtered version of PC_1^{SLP} , computed by taking a 24	
1192		month running mean. The red curve is $\langle \text{PC}_1^{\text{SLP}} \rangle$ plotted on top of PC_1^{SLP} . Note	
1193		that the $\langle \text{PC}_1^{\text{SLP}} \rangle$ time series shown in the third row has been normalized to	
1194		have a standard deviation of 1.	59
1195	9	Time lagged pattern correlations of Arctic sea ice in different regions. The	
1196		left column shows results from CCSM3 model output, and the right column	
1197		shows results from HadISST observations. All colored boxes are significant at	
1198		the 95% level, based on a t -test.	60
1199	10	Time lagged pattern correlations of sea ice computed over the Arctic domain,	
1200		using NLSA Families \mathcal{F}_1^M and \mathcal{F}_2^M . Panels (A) and (D) show correlations of the	
1201		raw data and \mathcal{F}_1^M , respectively. Panels (B) and (C) show cross-correlations of	
1202		\mathcal{F}_1^M and the raw data, with the NLSA data lagging and leading, respectively.	
1203		The same correlations for \mathcal{F}_2^M are shown in panels (E)-(H). All colored boxes	
1204		are significant at the 95% level.	61

- 1205 11 Time lagged pattern correlations of sea ice computed over the Arctic domain,
1206 using HadISST Family \mathcal{F}_1^O . Panels (A) and (D) show correlations of the
1207 raw data and NLSA Family \mathcal{F}_1^O , respectively. Panels (B) and (C) show cross-
1208 correlations of \mathcal{F}_1^O and the raw data, with the NLSA data lagging and leading,
1209 respectively. All colored boxes are significant at the 95% level. 62
- 1210 12 Time lagged patterns correlations of sea ice computed over the Arctic domain.
1211 Lagged correlations for CCSM3 data are shown for: (A) the raw data, (C)
1212 Raw - $\mathcal{F}_1^M - \mathcal{F}_2^M$, (E) conditional on $|L_1^{\text{SIC}}(t)| > 2$ or $|L_2^{\text{SIC}}(t)| > 2$ (which
1213 corresponds to 11% of the data) and (G) conditional on $|L_1^{\text{SIC}}(t)| < 1$ and
1214 $|L_2^{\text{SIC}}(t)| < 1$ (45% of the data). HadISST lagged correlations are shown for:
1215 (B) the raw data, (D) Raw - \mathcal{F}_1^O , (F) conditional on $|L_1^{\text{SIC}}(t)| > 1.5$ (which
1216 corresponds to 14% of the data) and (H) conditional on $|L_1^{\text{SIC}}(t)| < 1$ (59% of
1217 the data). 63
- 1218 13 Sea ice, SST, and SLP patterns of CCSM3 reemergence Family \mathcal{F}_1^M at differ-
1219 ent months of the year. These spatial patterns are composites, obtained by
1220 averaging over all years in which $L_1^{\text{SIC}} > 1$. 64
- 1221 14 Sea ice, SST, and SLP patterns of CCSM3 reemergence Family \mathcal{F}_2^M at differ-
1222 ent months of the year. These spatial patterns are composites, obtained by
1223 averaging over all years in which $L_2^{\text{SIC}} > 1$. 65
- 1224 15 Sea ice, SST, and SLP patterns of HadISST reemergence Family \mathcal{F}_1^O shown
1225 for different months of 1991. 66
- 1226 16 Reemergence metrics for ice, SST and wind of family \mathcal{F}_1^M in the Barents/Kara,
1227 Bering, and Labrador Seas, by which we judge the activity of ice reemergence.
1228 Active periods of reemergence are characterized by repeated years in which
1229 these metrics are large (either positive or negative). Note that the SIC and
1230 SST metrics have been normalized by their respective standard deviations.
1231 The SLP metric is reported in m/s. 67

- 1232 17 Reemergence metrics for ice, SST and wind of family \mathcal{F}_2^M in the Barents/Kara,
1233 Bering, and Labrador Seas, by which we judge the activity of ice reemergence.
1234 Active periods of reemergence are characterized by repeated years in which
1235 these metrics are large (either positive or negative). 68
- 1236 18 Reemergence metrics for ice, SST and wind of family \mathcal{F}_1^O in the Barents/Kara,
1237 Bering, and Labrador Seas, by which we judge the activity of ice reemergence.
1238 Active periods of reemergence are characterized by repeated years in which
1239 these metrics are large (either positive or negative). 69
- 1240 19 Lagged correlations in sea-ice area anomalies between different seas. (A) and
1241 (B) show CCSM3 correlations between the Barents-Kara and Bering Seas for
1242 the raw data and conditional on $|L_3^{\text{SLP}}| > 1.5$, respectively. (C) and (D) show
1243 CCSM3 correlations between the Bering and Labrador Seas for the raw data
1244 and conditional on $|L_1^{\text{SLP}}| > 1.5$, respectively. (E) and (F) show HadISST
1245 correlations between the Barents-Kara and Labrador Seas for the raw data
1246 and conditional on $|L_1^{\text{SLP}}| > 1$, respectively. 70

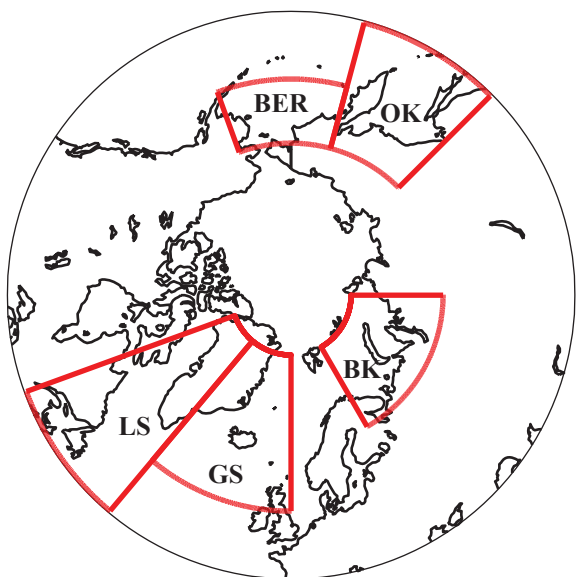


FIG. 1. The regions of interest in this study: the Barents-Kara Seas (BK), the Labrador Sea (LS), the Greenland Sea (GS), the Bering Sea (BER), and the Sea of Okhotsk (OK). The Arctic domain is defined as all grid points north of 45°N .

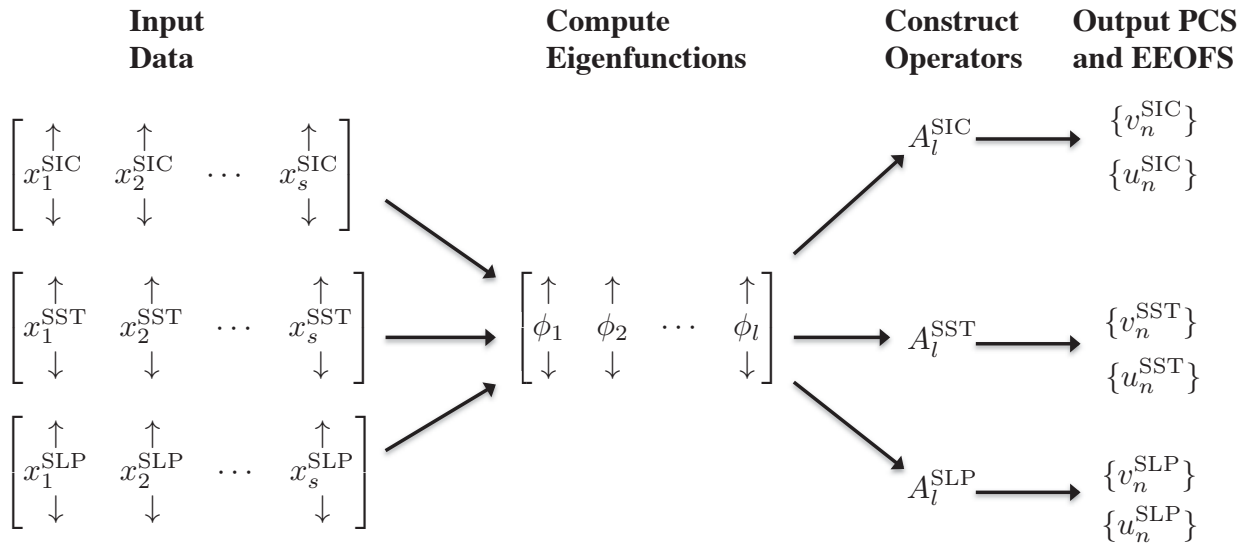


FIG. 2. Schematic summarizing the flow of data in the coupled NLSA algorithm.

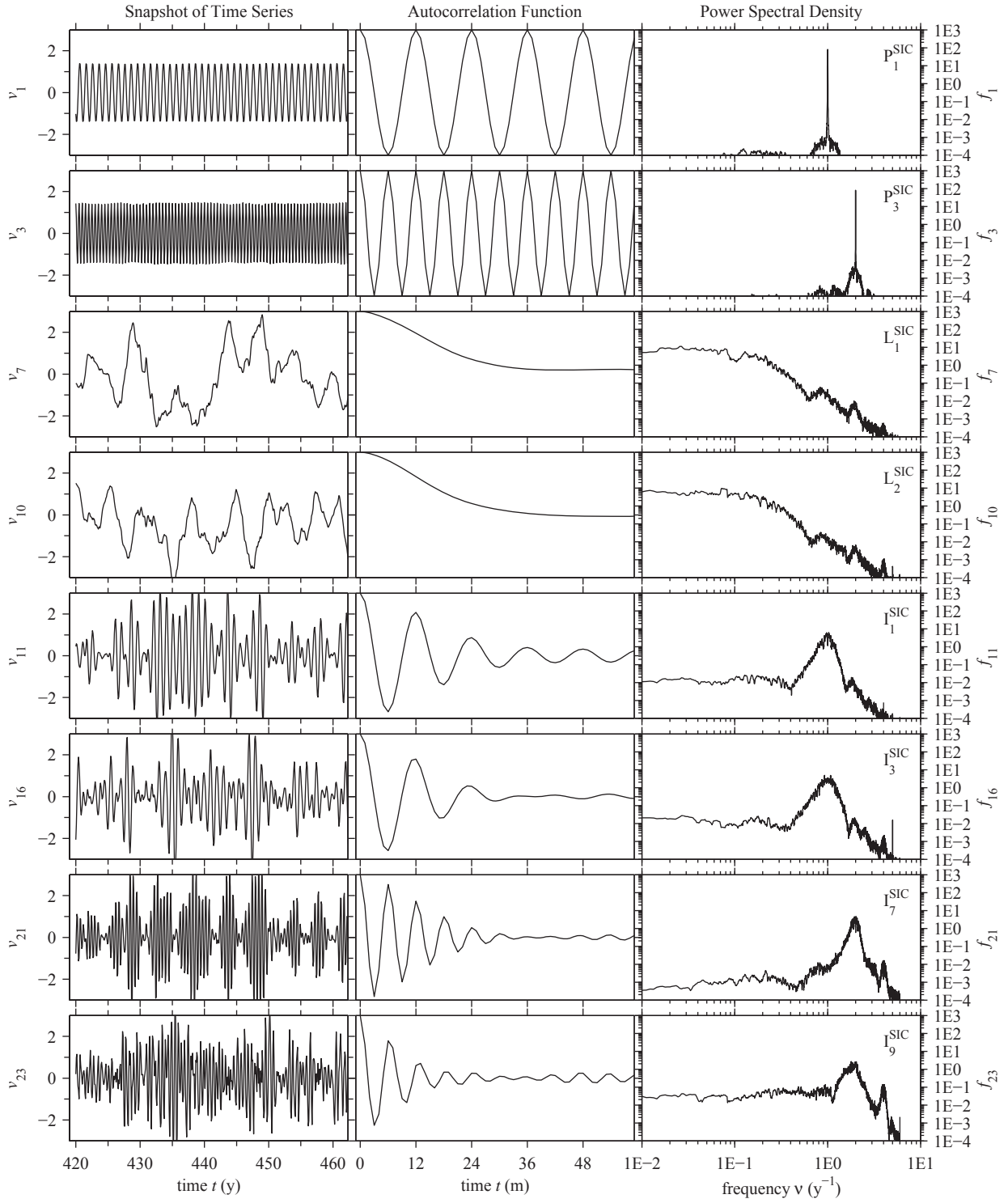


FIG. 3. Snapshots of the time series, power spectral density, and autocorrelation functions for the CCSM3 SIC PCs (v_k) from coupled NLSA. Shown here for 50-year portions of the 900-yr time series are the annual periodic (P_1^{SIC}) and semiannual periodic (P_3^{SIC}) modes, low-frequency modes (L_1^{SIC} and L_2^{SIC}), annual intermittent modes (I_1^{SIC} and I_3^{SIC}), and semiannual intermittent modes (I_7^{SIC} and I_9^{SIC}). The autocorrelation vertical scale is $[-1, 1]$. The power spectral densities (f_k) were estimated via the multitaper method with time-bandwidth product $p = 6$ and $K = 2p - 1 = 11$ Slepian ⁵⁴ tapers. The effective half-bandwidth resolution for the s monthly samples is $\Delta\nu = p/(s\delta t) = 1/150 \text{ y}^{-1}$, where $\delta t = 1/12 \text{ y}$ is the sampling interval.

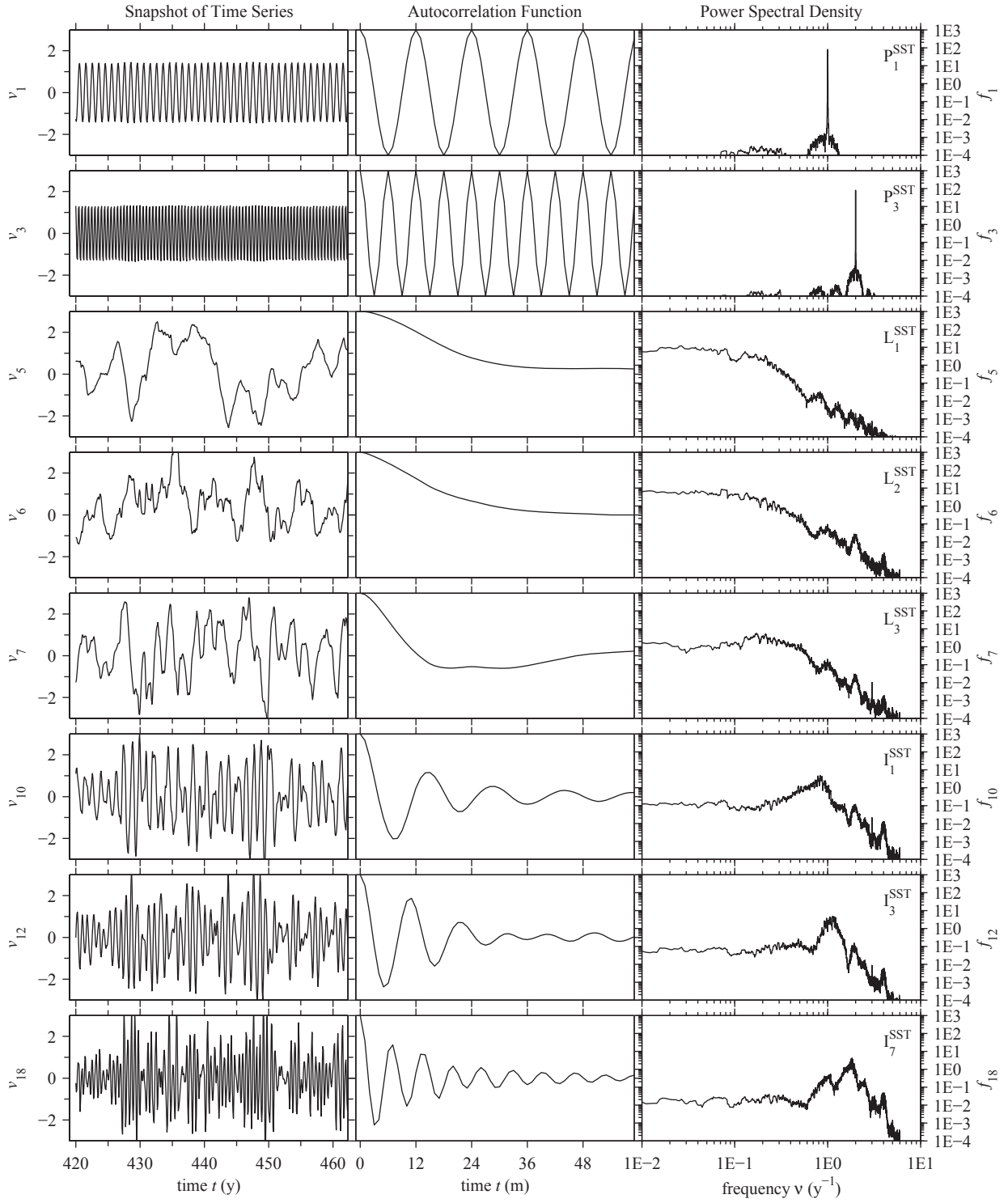


FIG. 4. Snapshots of the time series, power spectral density, and autocorrelation functions for the CCSM3 SST PCs from coupled NLSA. Shown here are the annual periodic (P_1^{SST}) and semiannual periodic (P_3^{SST}) modes, low-frequency modes (L_1^{SST} , L_2^{SST} , and L_3^{SST}), annual intermittent modes (I_1^{SST} and I_3^{SST}), and semiannual intermittent modes (I_7^{SST}). The autocorrelation vertical scale is $[-1,1]$.

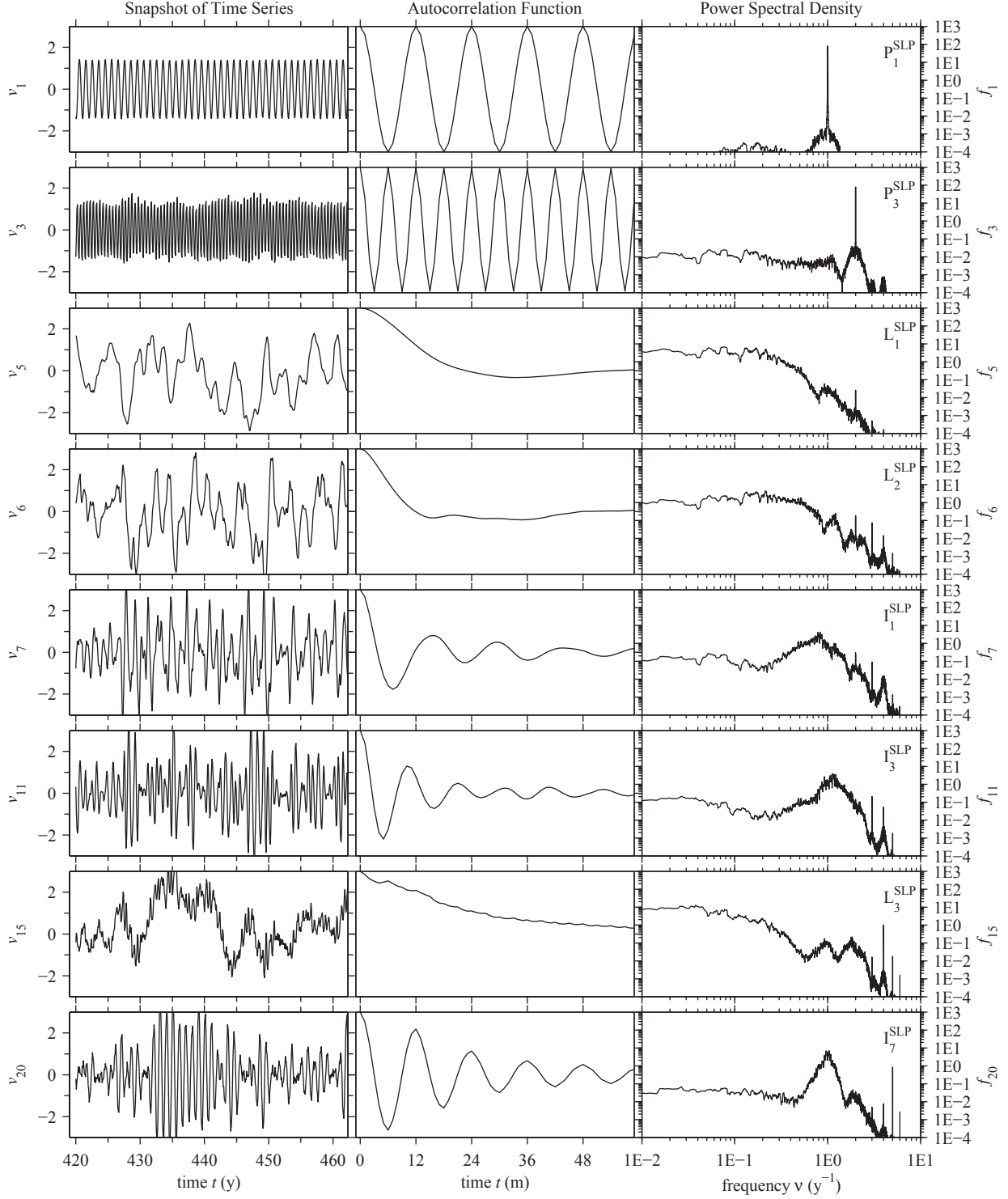


FIG. 5. Snapshots of the time series, power spectral density, and autocorrelation functions for the CCSM3 SLP PCs from coupled NLSA. Shown here are the annual periodic (P_1^{SLP}) and semiannual periodic (P_3^{SLP}) modes, low-frequency modes (L_1^{SLP} , L_2^{SLP} , L_3^{SLP}), and intermittent modes (I_1^{SLP} , I_3^{SLP} , I_7^{SLP}). The autocorrelation vertical scale is $[-1, 1]$.

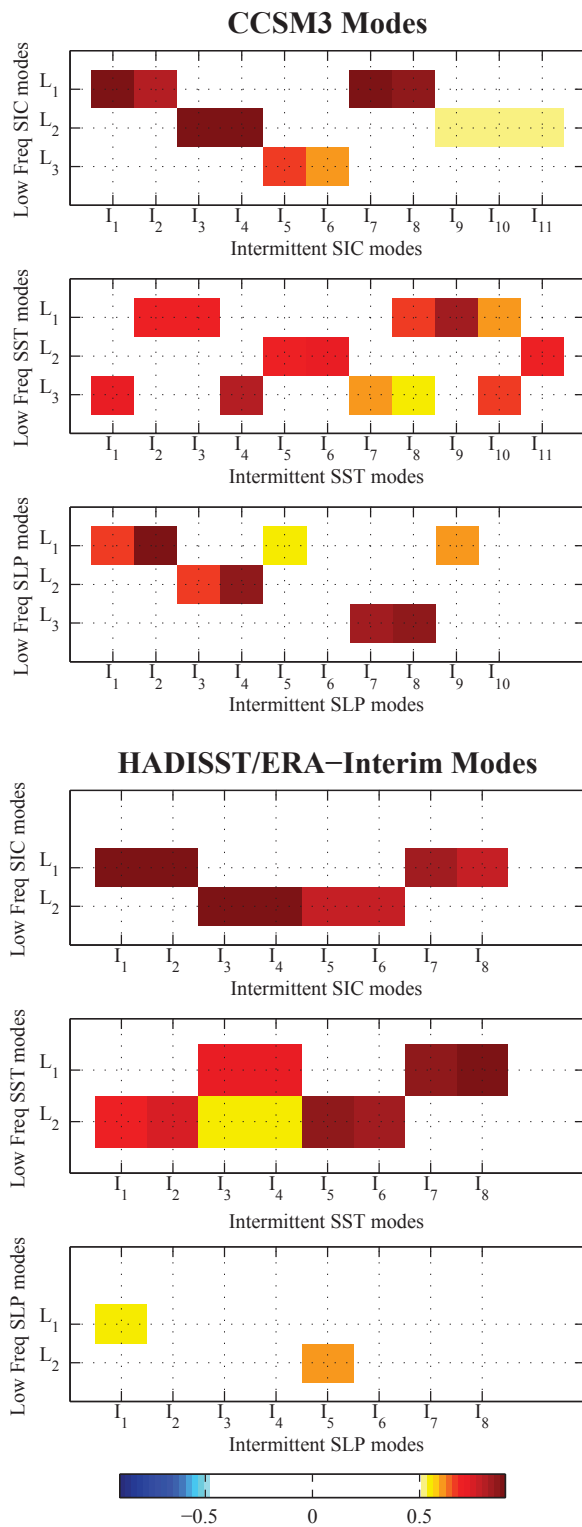


FIG. 6. Correlations between low-frequency modes and envelope functions for intermittent modes. Mode pairs with large positive correlations indicate that the low-frequency mode provides the modulating envelope for the intermittent mode.

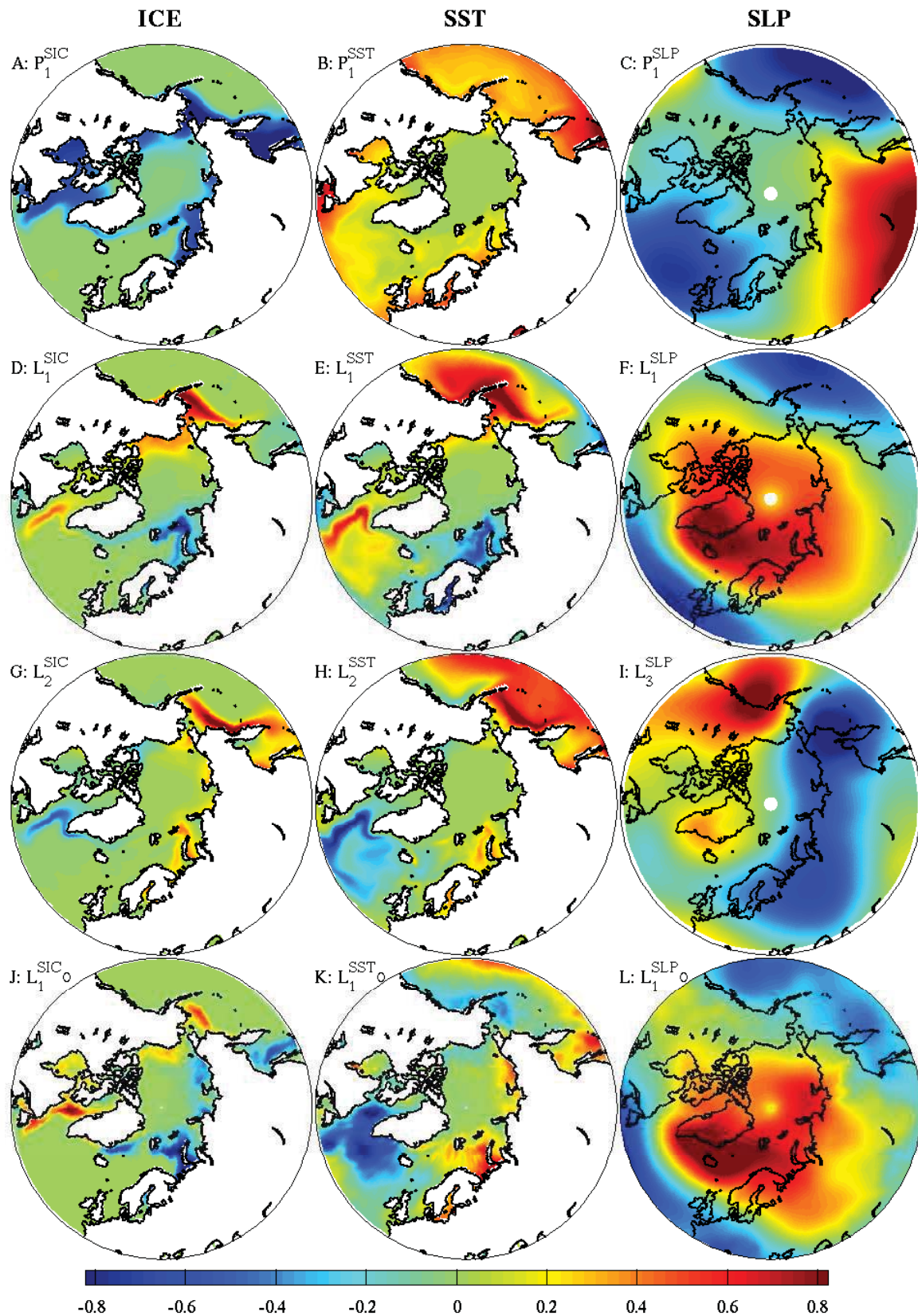


FIG. 7. Spatial patterns of selected sea ice, SST, and SLP NLSA modes. For each mode, we plot the spatial pattern with largest variance (of the q spatial patterns that make up the spatiotemporal pattern). Rows 1-3 show CCSM3 modes and row 4 shows observational modes, indicated by an O subscript. The fields have been normalized to have a maximum absolute value of 1.

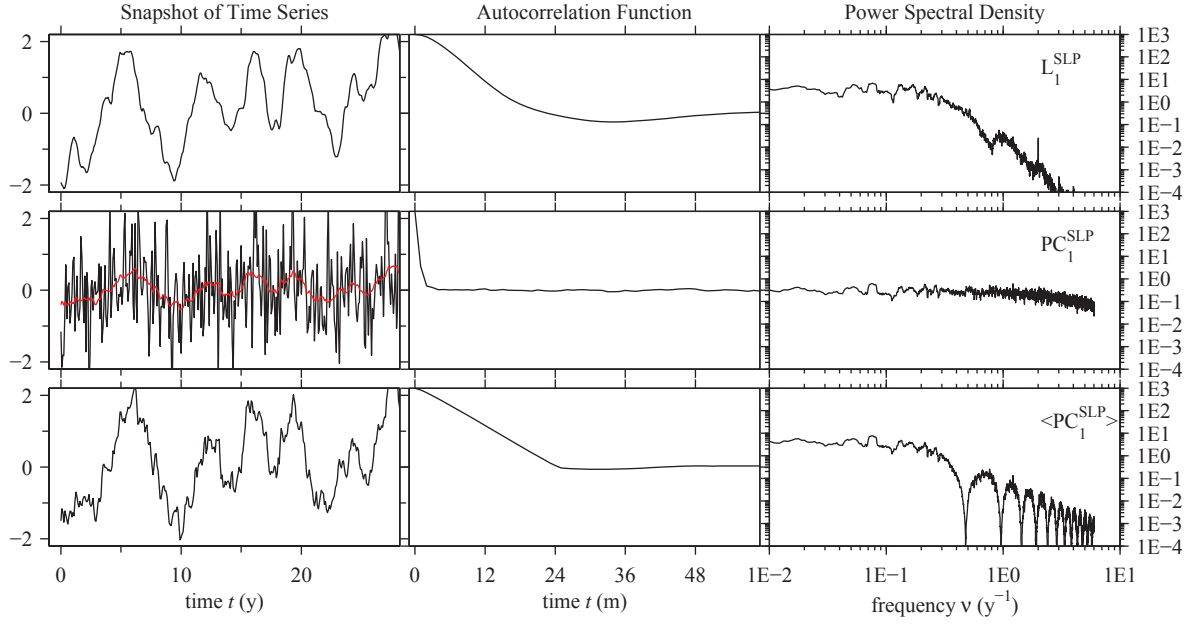


FIG. 8. Snapshots of the time series, power spectral density, and autocorrelation functions for L_1^{SLP} , the leading low-frequency NLSA mode from CCSM3, PC_1^{SLP} , the principal component corresponding to the leading EOF of SLP, and $\langle \text{PC}_1^{\text{SLP}} \rangle$, a low-pass filtered version of PC_1^{SLP} , computed by taking a 24 month running mean. The red curve is $\langle \text{PC}_1^{\text{SLP}} \rangle$ plotted on top of PC_1^{SLP} . Note that the $\langle \text{PC}_1^{\text{SLP}} \rangle$ time series shown in the third row has been normalized to have a standard deviation of 1.

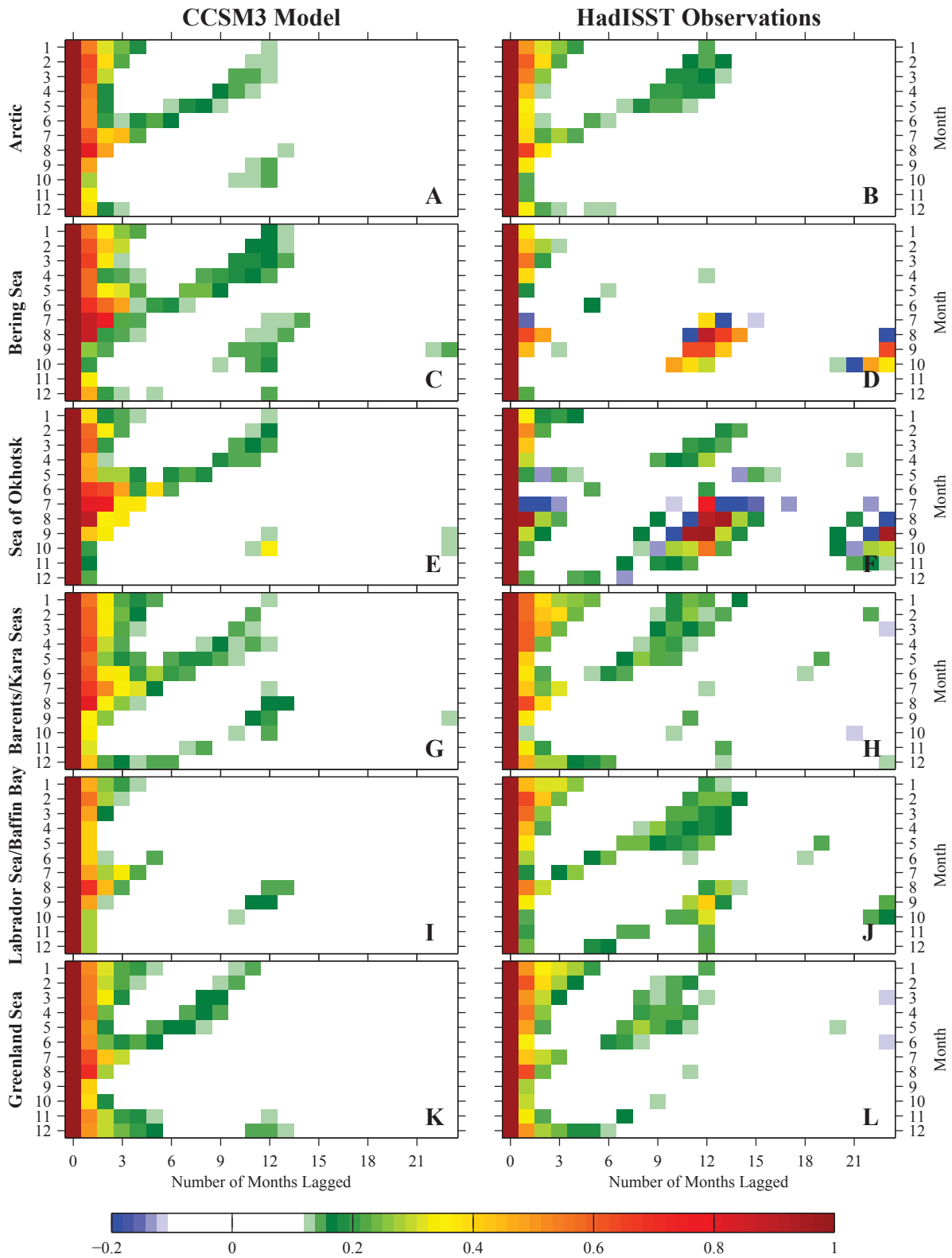


FIG. 9. Time lagged pattern correlations of Arctic sea ice in different regions. The left column shows results from CCSM3 model output, and the right column shows results from HadISST observations. All colored boxes are significant at the 95% level, based on a t -test.

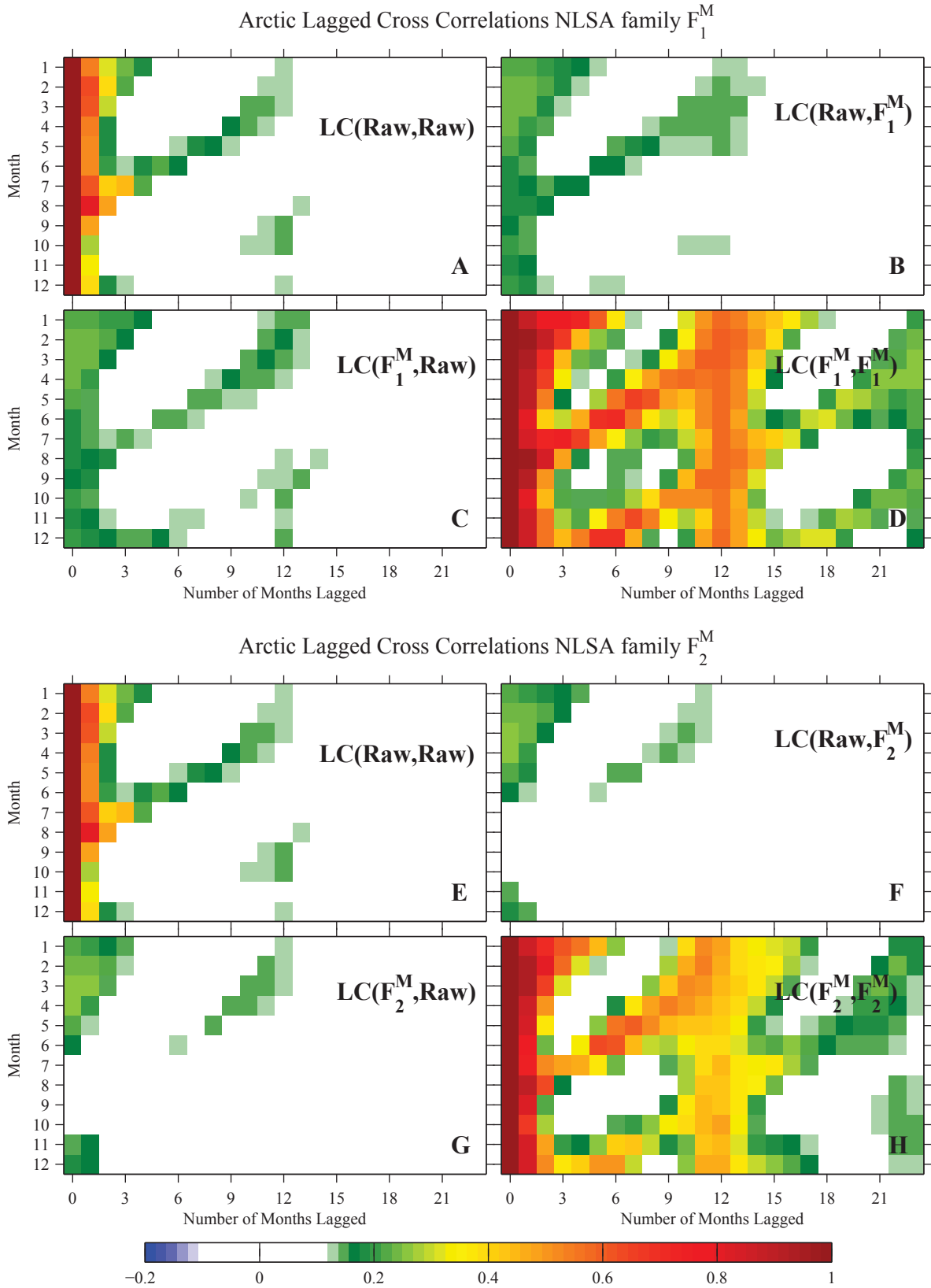


FIG. 10. Time lagged pattern correlations of sea ice computed over the Arctic domain, using NLSA Families \mathcal{F}_1^M and \mathcal{F}_2^M . Panels (A) and (G) show correlations of the raw data and \mathcal{F}_1^M , respectively. Panels (B) and (C) show cross-correlations of \mathcal{F}_1^M and the raw data, with the NLSA data lagging and leading, respectively. The same correlations for \mathcal{F}_2^M are shown in panels (E)-(H). All colored boxes are significant at the 95% level.

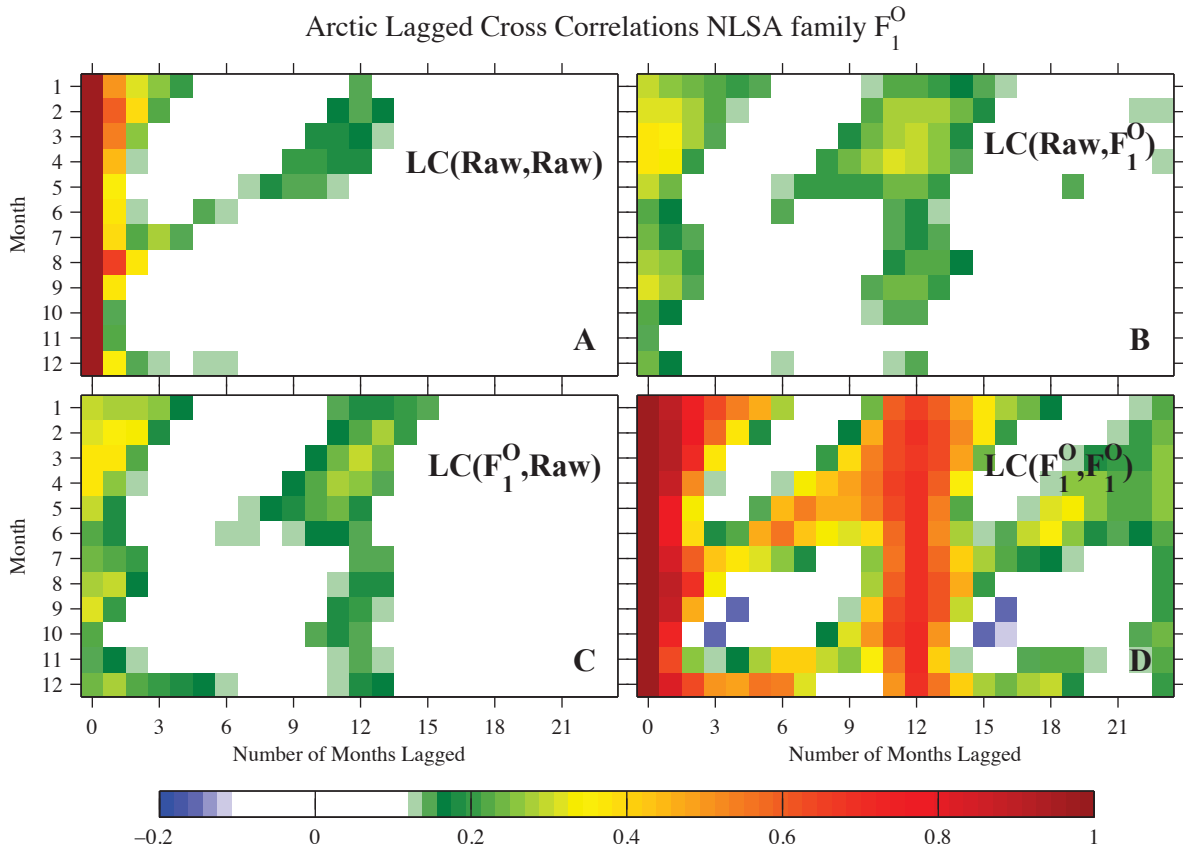


FIG. 11. Time lagged pattern correlations of sea ice computed over the Arctic domain, using HadISST Family \mathcal{F}_1^O . Panels (A) and (D) show correlations of the raw data and NLSA Family \mathcal{F}_1^O , respectively. Panels (B) and (C) show cross-correlations of \mathcal{F}_1^O and the raw data, with the NLSA data lagging and leading, respectively. All colored boxes are significant at the 95% level.

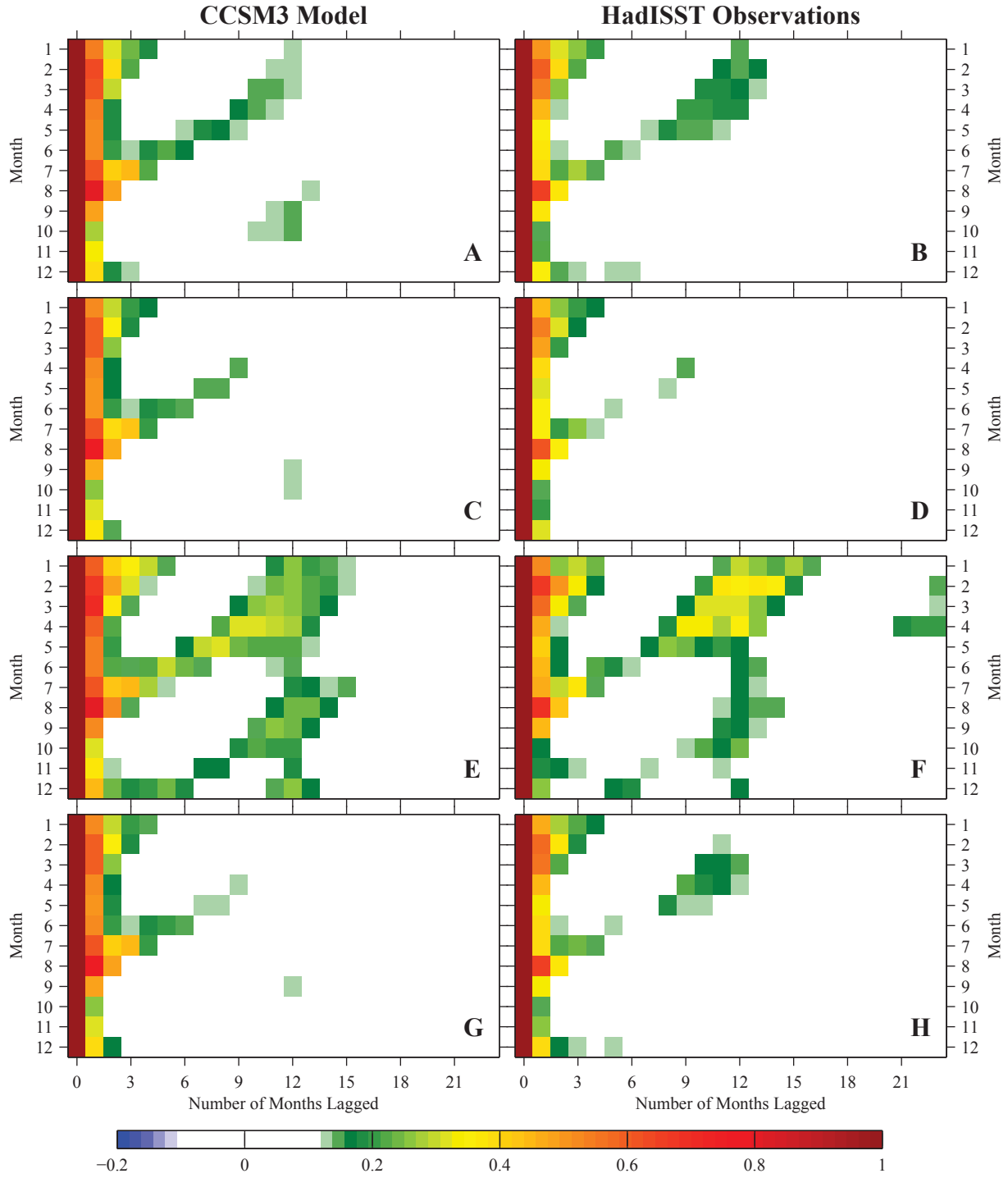
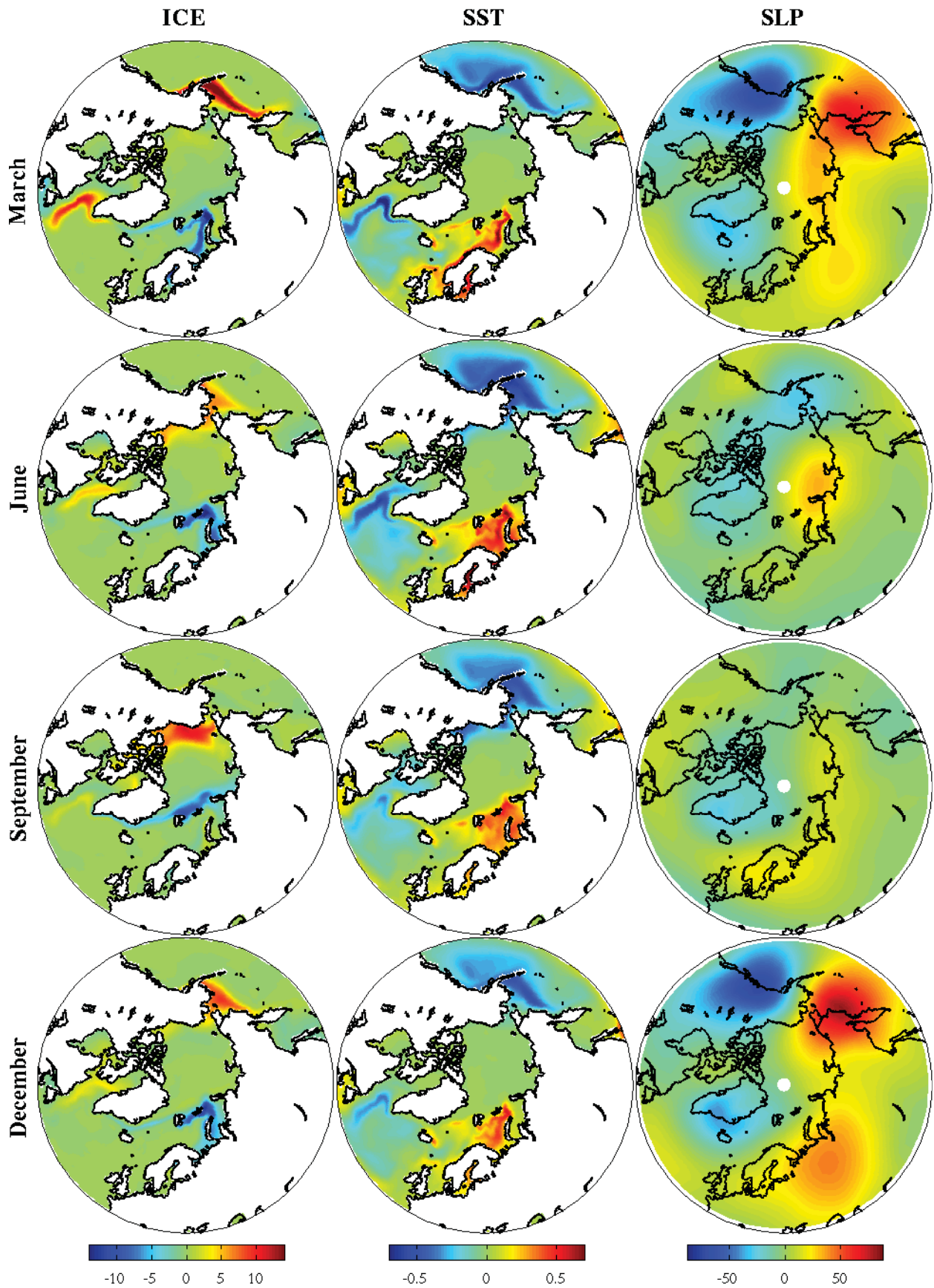
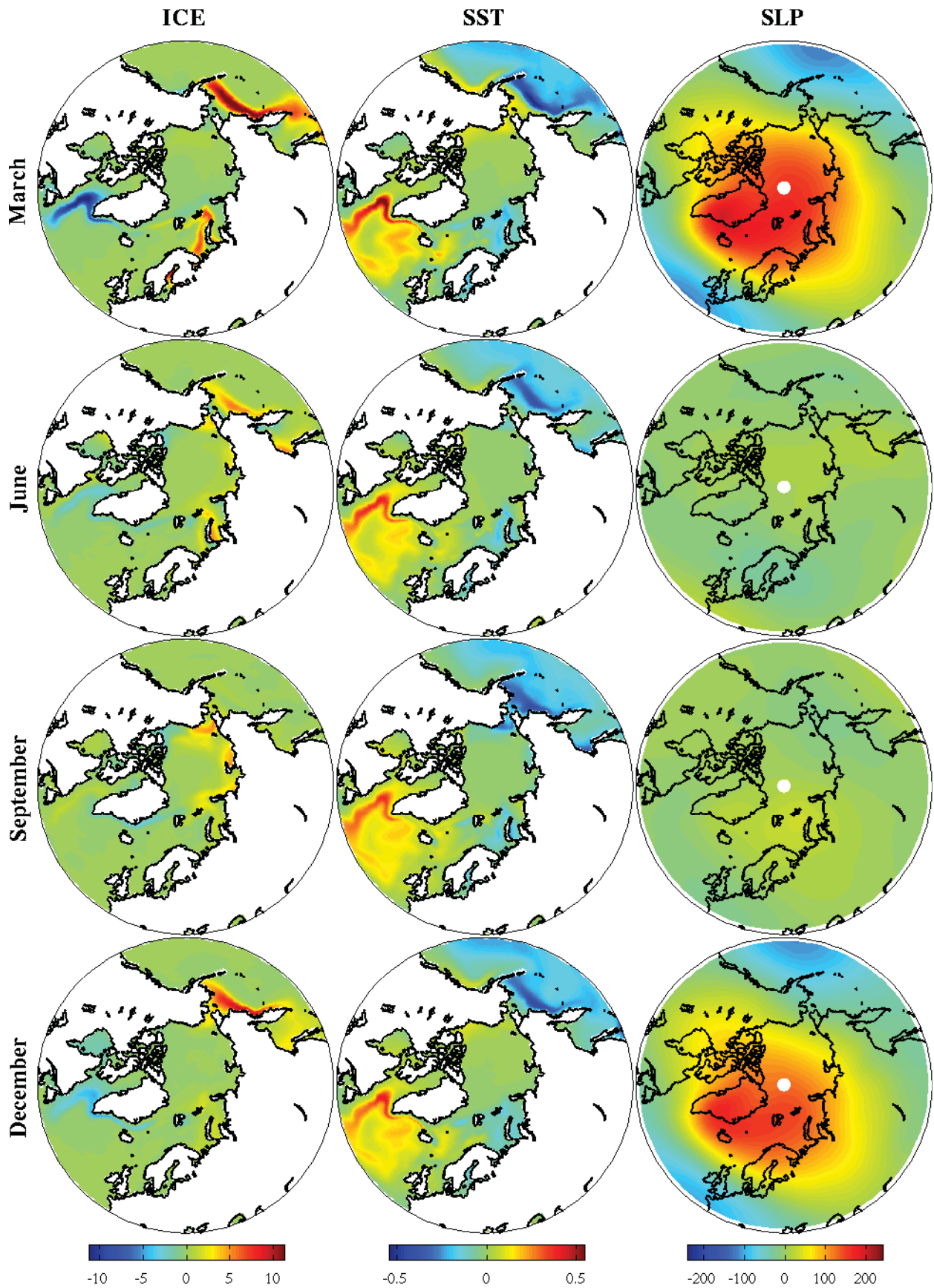


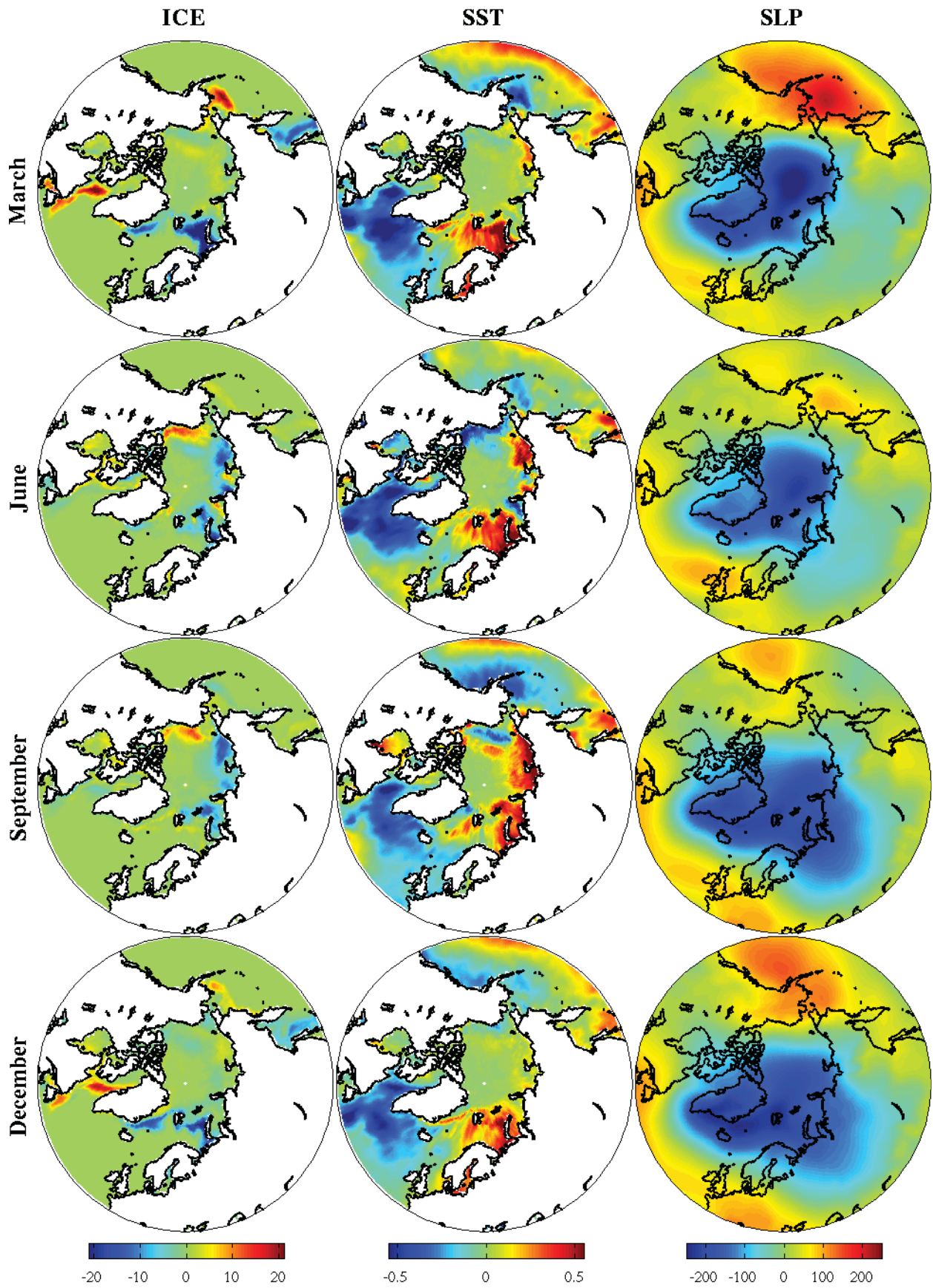
FIG. 12. Time lagged patterns correlations of sea ice computed over the Arctic domain. Lagged correlations for CCSM3 data are shown for: (A) the raw data, (C) $\text{Raw} - \mathcal{F}_1^M - \mathcal{F}_2^M$, (E) conditional on $|L_1^{\text{SIC}}(t)| > 2$ or $|L_2^{\text{SIC}}(t)| > 2$ (which corresponds to 11% of the data) and (G) conditional on $|L_1^{\text{SIC}}(t)| < 1$ and $|L_2^{\text{SIC}}(t)| < 1$ (45% of the data). HadISST lagged correlations are shown for: (B) the raw data, (D) $\text{Raw} - \mathcal{F}_1^O$, (F) conditional on $|L_1^{\text{SIC}}(t)| > 1.5$ (which corresponds to 14% of the data) and (H) conditional on $|L_1^{\text{SIC}}(t)| < 1$ (59% of the data).



64
 FIG. 13. Sea ice, SST, and SLP patterns of CCSM3 reemergence Family \mathcal{F}_1^M at different months of the year. These spatial patterns are composites, obtained by averaging over all years in which $L_1^{\text{SIC}} > 1$.



65
 FIG. 14. Sea ice, SST, and SLP patterns of CCSM3 reemergence Family \mathcal{F}_2^M at different months of the year. These spatial patterns are composites, obtained by averaging over all years in which $L_2^{\text{SIC}} > 1$.



66
 FIG. 15. Sea ice, SST, and SLP patterns of HadISST reemergence Family \mathcal{F}_1^O shown for different months of 1991.

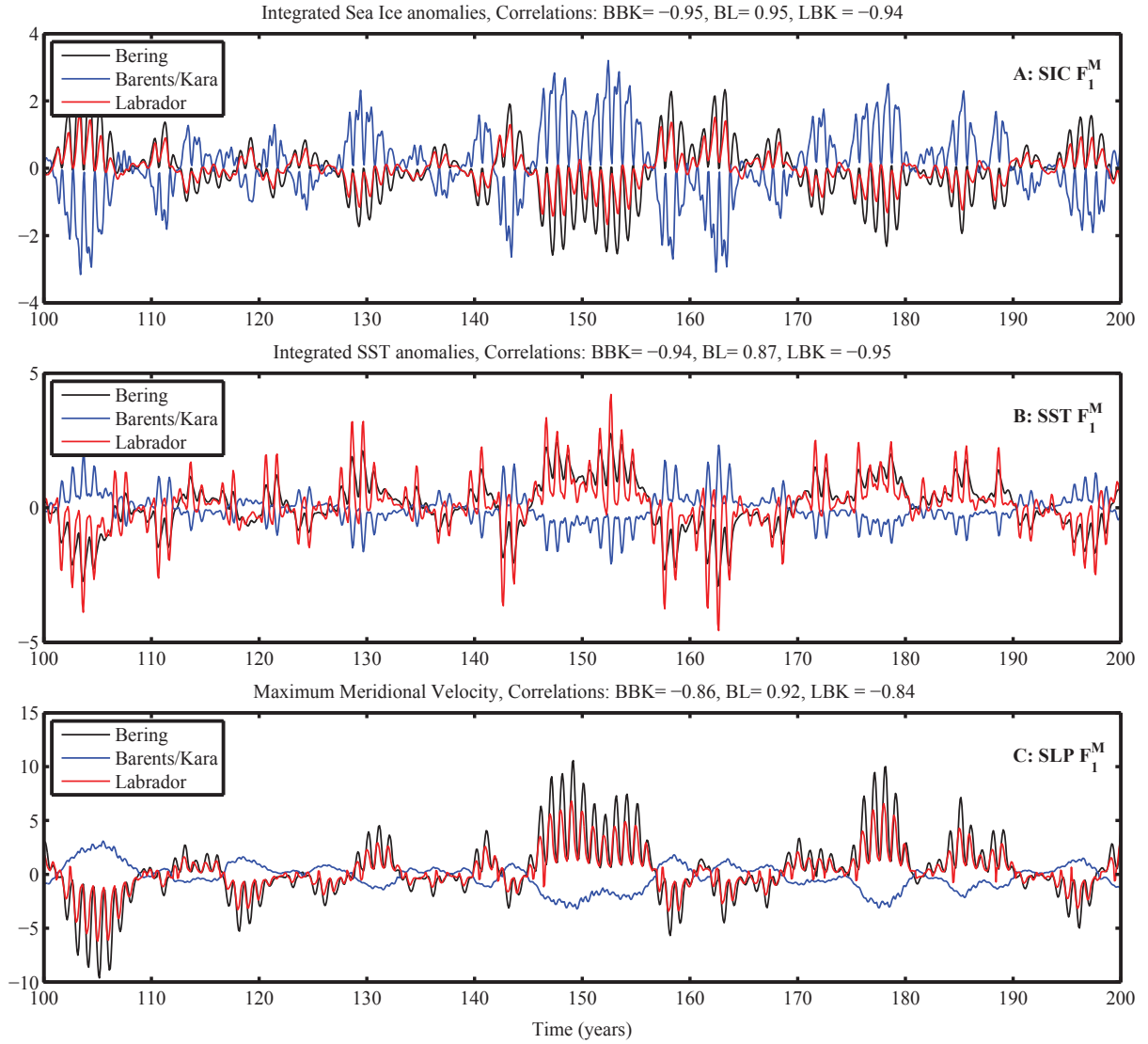


FIG. 16. Reemergence metrics for ice, SST and wind of family \mathcal{F}_1^M in the Barents/Kara, Bering, and Labrador Seas, by which we judge the activity of ice reemergence. Active periods of reemergence are characterized by repeated years in which these metrics are large (either positive or negative). Note that the SIC and SST metrics have been normalized by their respective standard deviations. The SLP metric is reported in m/s.

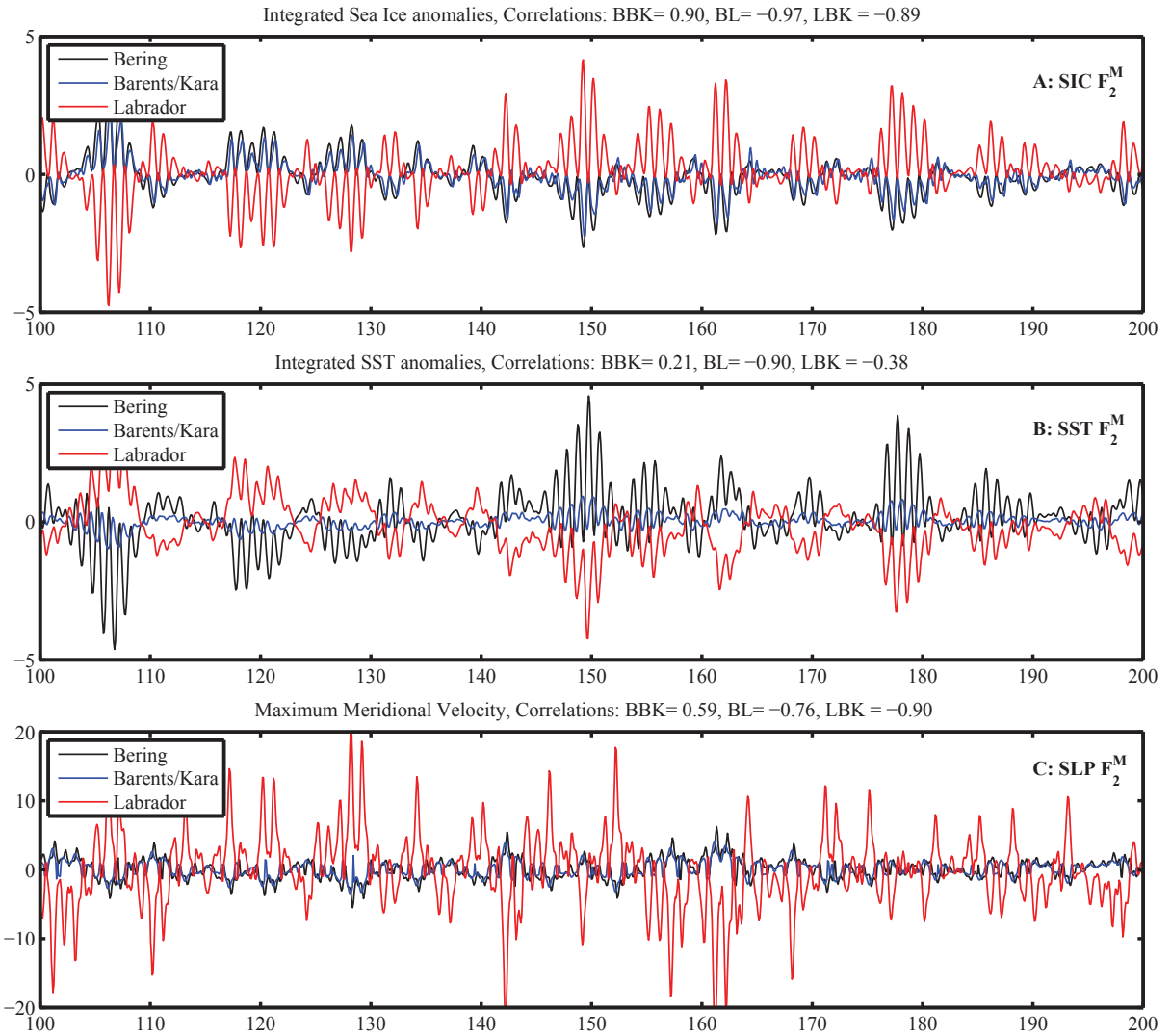


FIG. 17. Reemergence metrics for ice, SST and wind of family \mathcal{F}_2^M in the Barents/Kara, Bering, and Labrador Seas, by which we judge the activity of ice reemergence. Active periods of reemergence are characterized by repeated years in which these metrics are large (either positive or negative).

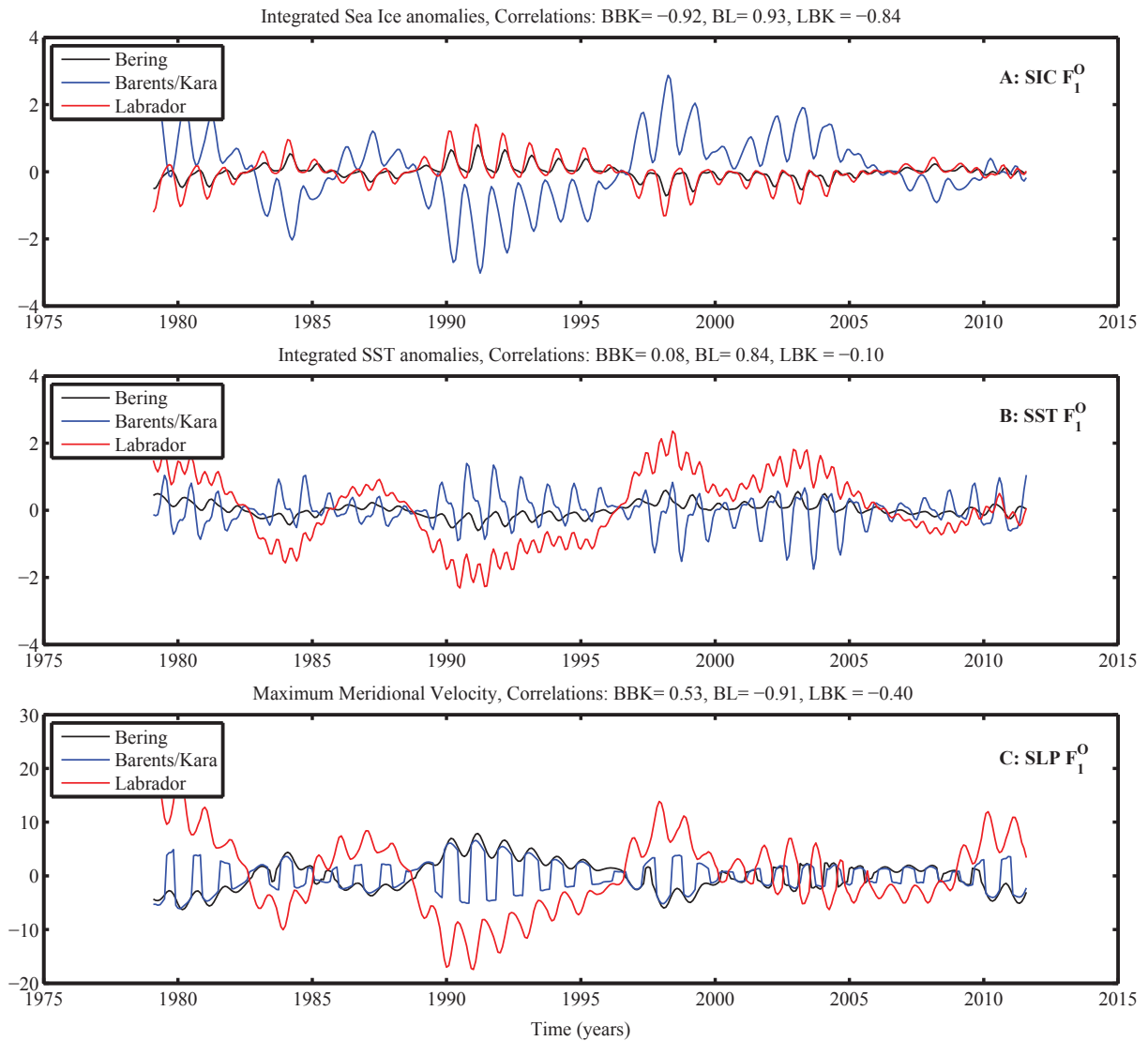


FIG. 18. Reemergence metrics for ice, SST and wind of family \mathcal{F}_1^O in the Barents/Kara, Bering, and Labrador Seas, by which we judge the activity of ice reemergence. Active periods of reemergence are characterized by repeated years in which these metrics are large (either positive or negative).

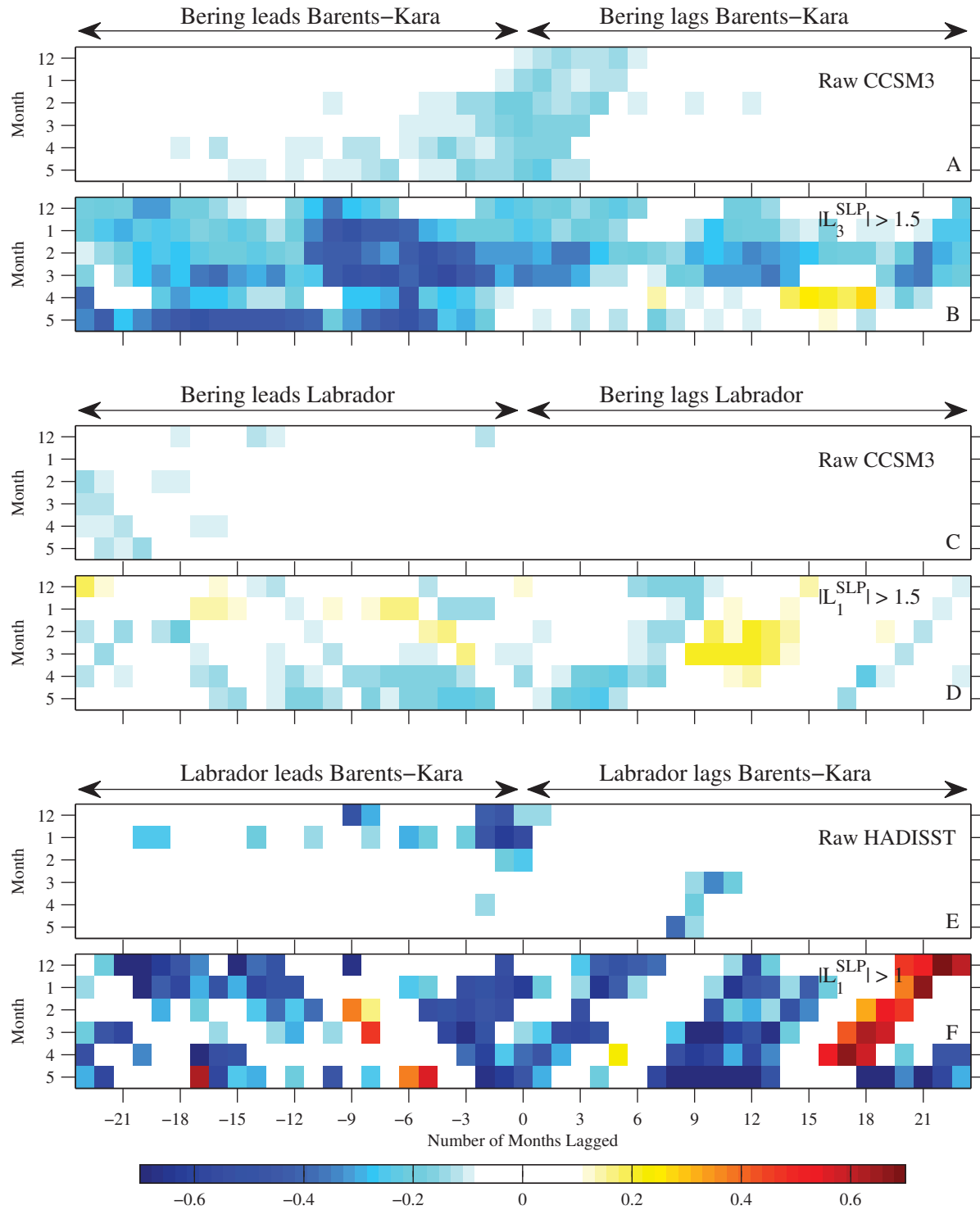


FIG. 19. Lagged correlations in sea-ice area anomalies between different seas. (A) and (B) show CCSM3 correlations between the Barents-Kara and Bering Seas for the raw data and conditional on $|L_3^{SLP}| > 1.5$, respectively. (C) and (D) show CCSM3 correlations between the Bering and Labrador Seas for the raw data and conditional on $|L_1^{SLP}| > 1.5$, respectively. (E) and (F) show HadISST correlations between the Barents-Kara and Labrador Seas for the raw data and conditional on $|L_1^{SLP}| > 1$, respectively.